Hydrodynamic interactions in the induced-charge electrophoresis of colloidal rod dispersions

By DAVID SAINTILLAN[1], ERIC DARVE[1,2]
AND ERIC S. G. SHAQFEH[1,2,3]

[1]Department of Mechanical Engineering, Stanford University, Stanford, CA 94305, USA

[2]Institute for Computational and Mathematical Engineering, Stanford University, Stanford, CA 94305, USA

[3]Department of Chemical Engineering, Stanford University, Stanford, CA 94305, USA

The behaviour of a dispersion of infinitely polarizable slender rods in an electric field is described using theory and numerical simulations. The polarization of the rods results in the formation of dipolar charge clouds around the particle surfaces, which in turn drive nonlinear electrophoretic flows under the action of the applied field. This induced-charge electrophoresis causes no net migration for uncharged particles with fore–aft symmetry, but can lead to rotations and to relative motions as a result of hydrodynamic interactions. A slender-body formulation is derived that accounts for induced-charge electrophoresis based on a thin double layer approximation, and shows that the effects of the electric field on a single rod can be modelled by a linear slip velocity along the rod axis, which causes particle alignment and drives a stresslet flow in the surrounding fluid. Based on this slender-body model, the hydrodynamic interactions between a pair of aligned rods are studied, and we identify domains of attraction and repulsion, which suggest that particle pairing may occur. An efficient method is implemented for the simulation of dispersions of many Brownian rods undergoing induced-charge electrophoresis, that accounts for far-field hydrodynamic interactions up to the stresslet term, as well as near-field lubrication and contact forces. Simulations with negligible Brownian motion show that particle pairing indeed occurs in the suspension, as demonstrated by sharp peaks in the pair distribution function. The superposition of all the electrophoretic flows driven on the rod surfaces is observed to result in a diffusive motion at long times, and hydrodynamic dispersion coefficients are calculated. Results are also presented for colloidal suspensions, in which Brownian fluctuations are found to hinder particle pairing and alignment. Orientation distributions are obtained for various electric field strengths, and are compared to an analytical solution of the Fokker–Planck equation for the orientation probabilities in the limit of infinite dilution.

1. Introduction

The manipulation of small particles suspended in a liquid is a challenging task, with applications in fields as diverse as separation science, analytical chemistry, micro-fluidics, or microrheology. A simple and widely used strategy for controlling particle motions consists of utilizing externally applied electric fields, which under certain conditions can cause particle migration and reorientation. The basic mechanism for

this electrophoretic motion has been described extensively, and falls into the broad category of linear electrokinetic phenomena (e.g. Saville 1977; Russel, Saville & Schowalter 1989; Hiemenz & Rajagopalan 1997; Hunter 2001). A uniformly charged surface in an electrolyte attracts a cloud of counterions, which accumulate near the surface, resulting in the formation of an electrical double layer (EDL). The application of a steady electric field exerts a net force on the excess counterions, which migrate along the local electric field lines and drag the fluid with them. Near a fixed surface such as a channel wall, this effective body force inside the EDL drives an electro-osmotic flow in the fluid bulk. In the case of a freely suspended particle such as a colloid or macromolecule, electrophoretic migration occurs.

When the characteristic thickness λ_D of the EDL is much less than the characteristic radius of curvature of the particle, and if the applied field is sufficiently weak for surface conduction to be negligible, a boundary layer analysis of the electrokinetic and flow equations shows that to a good approximation the effects of the body force on the charge cloud can be captured by an effective slip velocity $\boldsymbol{u}_s$ at the outer edge of the EDL, given by the Helmholtz–Smoluchowski equation:

$$\boldsymbol{u}_s = -\frac{\varepsilon\zeta}{\mu}\boldsymbol{E}_s, \tag{1.1}$$

where ε and μ are the permittivity and viscosity of the fluid, respectively, and $\boldsymbol{E}_s$ is the value of the electric field at the edge of the EDL, where it is tangential to the local surface. The parameter ζ, called zeta-potential, is the electric potential drop across the double layer, and is considered a material property. The Helmholtz–Smoluchowski equation (1.1) can be used as a boundary condition for the flow equations outside the charge cloud. For a freely suspended spherical particle this slip boundary condition was shown by Smoluchowski (1903) and Henry (1931) to yield the following translational velocity in an applied field $\boldsymbol{E}_\infty$:

$$\boldsymbol{U} = \frac{\varepsilon\zeta}{\mu}\boldsymbol{E}_\infty. \tag{1.2}$$

This classical result, which assumes a spherical shape, uniform charge density, absence of polarization, thin electrical double layer and weak applied field, was later generalized to more complex situations. First Morrison (1970) proved that the same result holds for any particle shape under the same assumptions, and that the torque on a non-spherical particle is zero. O'Brien (1983) and O'Brien & Ward (1988) considered the effects of surface conduction, which results from charge build-up in some regions of the EDL and can be significant when the applied field is not weak or as the zeta-potential increases. Ion transport within the EDL was also addressed by Solomentsev, Pawar & Anderson (1993), who also accounted for a non-uniform surface charge density. Solomentsev & Anderson (1995) studied the effects of non-homogeneous electric fields, and showed that electric field gradients cause rotation, while second gradients contribute to translation without rotation. A variety of non-spherical particle shapes have also been considered, including spheroids (O'Brien & Ward 1988; Fair & Anderson 1989; Solomentsev & Anderson 1995), disks (Sherwood & Stone 1995), rod-like particles (Han & Yang 1996; Chen & Koch 1996), and slender bodies (Solomentsev & Anderson 1994; Sellier 2000).

While many investigations have addressed the case of particles with a fixed, possibly non-uniform, charge density, the present paper considers particles that can acquire a surface charge by polarization. Typical examples include polarizable dielectric particles and metallic colloids, which recently have found applications in analytical

chemistry and biological assays (e.g. Nicewarner-Peña *et al.* 2001; Walton *et al.* 2002). The behaviour of polarizable colloids in an electric field was previously studied in a series of papers by Dukhin and coworkers (Gamayunov, Murtsovkin & Dukhin 1986; Dukhin & Murtsovkin 1986; Dukhin 1986), the results of which were later summarized by Murtsovkin (1996). As explained in these papers, the polarization of a suspended sphere due to an applied electric field results in the formation of a dipolar charge cloud similar to the electrical double layer of classical electrophoresis, the effects of which can be modelled by an effective non-uniform zeta-potential. The action of the electric field on this charge cloud in turn drives a nonlinear electrophoretic flow around the particle: this flow, which has a quadrupolar structure, does not lead to a net particle motion in the case of a sphere, but can create relative motions between nearby particles as a result of hydrodynamic interactions. Experimental observations of this induced flow were reported by Gamayunov, Mantrov & Murtsovkin (1992) and recently by Levitan *et al.* (2005).

The general framework for the modelling of these flows was laid out in detail in the context of fixed electrodes in microfluidic devices by Bazant & Squires (2004) and Squires & Bazant (2004), who named the phenomenon induced-charge electro-osmosis. The terminology of induced-charge electrophoresis was also proposed in the case of freely suspended particles. More recently, Squires & Bazant (2006) considered a variety of situations where broken symmetries in induced-charge electrophoresis (such as shape anisotropy, non-uniform surface properties, or non-uniform applied fields) can result in particle motions. An important conclusion of their work is that shape anisotropy can yield quite different behaviours than in the case of perfectly spherical particles: departures from sphericity indeed result in the rotation and alignment of the particle in the direction of the electric field, while shape asymmetry can lead to the migration of a particle carrying no net charge. Some of these effects were also described recently by Yariv (2005), who derived general formulae for the linear and angular velocities of a particle of arbitrary shape.

In this work we focus on the effects of hydrodynamic interactions on the particle dynamics in suspensions of infinitely polarizable slender rods undergoing induced-charge electrophoresis. In particular, we wish to determine how the induced electrophoretic flows on the particle surfaces influence statistical properties such as orientation probabilities, pair probabilities, and hydrodynamic diffusivities in suspensions of hydrodynamically interacting particles. We start by considering the case of a single particle in §2, where we derive a simple slender-body formulation that captures the effects of the induced-charge electrophoresis on both the particle dynamics and the surrounding fluid flow. This slender-body model combined with the method of reflections is used to investigate pair interactions in suspensions of aligned rods in §3. To obtain more quantitative information on the behaviour of systems of many particles, we describe in §4 a method for the simulation of periodic systems of interacting rods that accounts for induced-charge electrophoresis, far-field and near-field hydrodynamic interactions, and Brownian motion. Simulation results are presented for both non-Brownian and Brownian suspensions in §5, where orientation probabilities, pair probabilities, and hydrodynamic dispersion are all discussed in detail. A summary and concluding remarks are given in §6.

2. Induced-charge electrophoresis of a polarizable rod

The basic theory and formalism for induced-charge electrokinetic phenomena were discussed in detail in the case of an infinite cylinder by Squires & Bazant (2004),
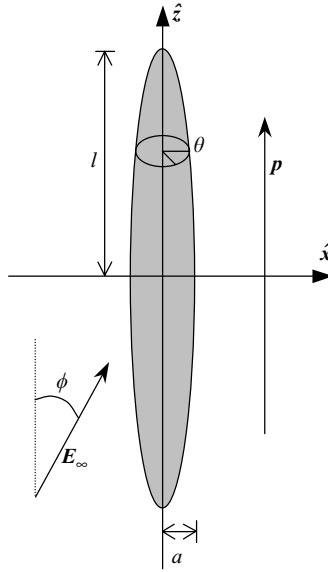
FIGURE 1. Problem geometry: the major axis of the spheroid, denoted by a unit vector $\boldsymbol{p}$, is assumed to be aligned in the z-direction, and forms an angle ϕ with respect to the direction of the applied electric field: $\boldsymbol{E}_\infty \cdot \boldsymbol{p} = E_\infty \cos \phi$. The azimuthal angle in the (x,y)-plane is denoted by θ.

who also justified them using an asymptotic analysis. In §2.1 we present an extension of their theory to the case of a polarizable rod-like particle, which for simplicity we take to be a spheroid. The limit of high aspect ratio, which is examined in §2.2 and §2.3, will yield results that are independent of the exact shape of the particle. Focus is placed on the derivation of a simple model that encompasses the electrophoretic motion of the particle while capturing the induced hydrodynamic interactions.

2.1. *Basic theory*

Consider a conducting polarizable spheroid in an electrolyte, to which an electric field $\boldsymbol{E}_\infty$ is applied as shown in figure 1. We define a coordinate system such that the major axis of the spheroid, whose direction is given by a unit vector $\boldsymbol{p}$, lies along the z-direction, and without loss of generality we can assume that both vectors $\boldsymbol{E}_\infty$ and $\boldsymbol{p}$ lie in the (x,z)-plane and form an angle ϕ: $\boldsymbol{E}_\infty \cdot \boldsymbol{p} = E_\infty \cos \phi$. Let $2l$ and $2a$ be the lengths of the major and minor axes of the spheroid, respectively. We denote by γ the particle aspect ratio, and by α its inverse, which will prove to be a useful quantity in the following discussion:

$$\gamma = \alpha^{-1} = l/a. \tag{2.1}$$

We also introduce an abscissa $s \in [-l, l]$ along the axis of the particle and a cylindrical coordinate system (r, θ, z) where $r^2 = x^2 + y^2$ and θ is the azimuthal angle in the (x, y)-plane, and let $\boldsymbol{x} = r\hat{\boldsymbol{r}} + z\hat{\boldsymbol{z}}$ denote a general position vector. With these definitions the equation for the surface ∂S of the spheroid can be written as

$$\frac{x^2 + y^2}{a^2} + \frac{z^2}{l^2} = \frac{r^2}{a^2} + \frac{z^2}{l^2} = 1. \tag{2.2}$$

2.1.1. *Electric problem*

When placed in a uniform electric field, a conducting particle modifies the field in such as way that the field lines intersect its surface at right angles. In a net neutral medium, the electric potential Φ therefore satisfies Laplace's equation:

$$\nabla^2 \Phi = 0, \tag{2.3}$$

subject to the conducting boundary conditions:

$$\left.\begin{array}{ll} \Phi(\boldsymbol{x}) = \Phi_s & \text{as } \boldsymbol{x} \in \partial S, \\ \nabla\Phi(\boldsymbol{x}) \to -\boldsymbol{E}_\infty & \text{as } |\boldsymbol{x}| \to \infty, \end{array}\right\} \tag{2.4}$$

where Φ_s is the uniform potential of the particle. As argued however by Squires & Bazant (2004), this configuration is not stable as the electric field in the electrolyte results in the migration of ions along the field lines with a current $\boldsymbol{J} = \sigma \boldsymbol{E}$ (where σ is the conductivity of the solution). These ions accumulate on the surface of the particle which itself polarizes, resulting in the formation of a dipolar charge cloud similar in nature to the electrical double layer of classical electro-osmosis. The double layer, which is net neutral, has the effect of repelling the electric field lines so that at steady state the particle and its EDL behave like an insulator.

In the following discussion we make the assumptions of thin EDL and weak applied fields. The first assumption states that the characteristic thickness λ_D of the double layer is much less than the characteristic radius of curvature of the particle:

$$\frac{\lambda_D}{a} \ll 1. \tag{2.5}$$

For a symmetric electrolyte the thickness λ_D, or Debye screening length, is defined as

$$\lambda_D \equiv \sqrt{\frac{\varepsilon kT}{2n_0(ze)^2}}, \tag{2.6}$$

where ε is the electric permittivity of the electrolyte, k is Boltzmann's constant, T is the absolute temperature, n_0 is the ionic concentration in the bulk of the electrolyte, and ze is the charge of a single ion. Under the thin EDL assumption a boundary layer approximation can be used to derive new boundary conditions for the electric field that apply at the edge of the EDL. Note that the thin EDL assumption is rather severe in the case of slender particles addressed here, since the particle thickness a can be quite small: it is likely therefore to apply only at relatively high salt concentrations, for which the Debye screening length is very small, or for mesoscopic or macroscopic particles, whose thickness a remains relatively large. In other cases the effects of finite EDL thickness are likely to come into play, and would require a different treatment. Finally, the weak applied field condition, or Debye–Hückel approximation, can be stated as $E_\infty a \ll kT/ze$ and ensures that surface conduction can be neglected.

Under these assumptions the boundary conditions equation (2.4) can be replaced by the following insulating boundary conditions:

$$\left.\begin{array}{ll} \boldsymbol{n} \cdot \nabla\Phi(\boldsymbol{x}) = 0 & \text{as } \boldsymbol{x} \in \partial S, \\ \nabla\Phi(\boldsymbol{x}) \to -\boldsymbol{E}_\infty & \text{as } |\boldsymbol{x}| \to \infty, \end{array}\right\} \tag{2.7}$$

where $\boldsymbol{n}$ is a unit outward normal on the particle surface. Equation (2.7) technically applies at the outer edge of the boundary layer, but can be safely enforced on the particle surface as we assumed that the Debye length is much less than the radius of the particle. This boundary condition, which can be justified by matched asymptotics

(Squires & Bazant 2004), results in electric field lines that are everywhere tangential to the particle surface.

Equations (2.3) and (2.7) for a spheroid admit an analytical solution, which can be obtained by the method of singularities (Chwang & Wu 1974, 1975; Han & Yang 1996). The electric field outside the spheroid is sought as that due to a line distribution of potential dipoles along the focal axis:

$$\boldsymbol{E}(\boldsymbol{x}) = \left\{ \boldsymbol{I} + \int_{-c}^{c} (c^2 - s^2)[\beta_{\parallel} \boldsymbol{D}(\boldsymbol{x} - s\hat{\boldsymbol{z}}; \hat{\boldsymbol{z}})\hat{\boldsymbol{z}} + \beta_{\perp} \boldsymbol{D}(\boldsymbol{x} - s\hat{\boldsymbol{z}}; \hat{\boldsymbol{x}})\hat{\boldsymbol{x}}] \, \mathrm{d}s \right\} \cdot \boldsymbol{E}_{\infty}; \qquad (2.8)$$

$c = (l^2 - a^2)^{1/2}$ is the half-focal length of the spheroid, and $\boldsymbol{D}(\boldsymbol{x}; \boldsymbol{a})$ is the field induced by a three-dimensional potential dipole of strength $\boldsymbol{a}$:

$$\boldsymbol{D}(\boldsymbol{x}; \boldsymbol{a}) = \nabla \left(\nabla \cdot \frac{\boldsymbol{a}}{x} \right) = -\frac{\boldsymbol{a}}{x^3} + 3\frac{(\boldsymbol{a} \cdot \boldsymbol{x})\boldsymbol{x}}{x^5}. \qquad (2.9)$$

Equation (2.8) satisfies Laplace's equation by construction. The integral can be computed analytically (Chwang & Wu 1975), and enforcing the boundary condition at the surface ($\boldsymbol{n} \cdot \boldsymbol{E}(\boldsymbol{x}) = 0$) allows one to solve for the constants $\beta_{\parallel}$ and $\beta_{\perp}$:

$$\beta_{\parallel} = \alpha^2 \left[-4(1 - \alpha^2)^{1/2} + 2\alpha^2 \log \left(\frac{1 + (1 - \alpha^2)^{1/2}}{1 - (1 - \alpha^2)^{1/2}} \right) \right]^{-1}, \qquad (2.10)$$

$$\beta_{\perp} = \alpha^2 \left[2(1 - \alpha^2)^{1/2} - 4(1 - \alpha^2)^{3/2} - 2\alpha^2 \log \left(\frac{1 + (1 - \alpha^2)^{1/2}}{1 - (1 - \alpha^2)^{1/2}} \right) \right]^{-1}. \qquad (2.11)$$

After manipulation, the electric field and potential on the surface of the spheroid are found to be

$$\boldsymbol{E}_s = (\boldsymbol{I} - \boldsymbol{nn}) \cdot \boldsymbol{G} \cdot \boldsymbol{E}_{\infty}, \qquad (2.12)$$

$$\Phi_s = -\boldsymbol{x} \cdot \boldsymbol{G} \cdot \boldsymbol{E}_{\infty}. \qquad (2.13)$$

$\boldsymbol{G}$ is the following geometric tensor:

$$\boldsymbol{G} = G_{\parallel} \hat{\boldsymbol{z}}\hat{\boldsymbol{z}} + G_{\perp}(\boldsymbol{I} - \hat{\boldsymbol{z}}\hat{\boldsymbol{z}}), \qquad (2.14)$$

with

$$G_{\parallel} = -2\frac{(1 - \alpha^2)^{3/2}}{\alpha^2}\beta_{\parallel}, \quad G_{\perp} = -4\frac{(1 - \alpha^2)^{3/2}}{\alpha^2}\beta_{\perp}. \qquad (2.15)$$

Equations (2.10)–(2.15) are equivalent to those given by Stratton (1941) and Fair & Anderson (1989), which were obtained using ellipsoidal harmonics. Figure 2 shows typical field lines in the (x,z)-plane calculated for various orientations of the electric field. Note that these field lines differ substantially from those obtained in two dimensions, by conformal mapping for instance, especially when the field is not aligned with the direction of the major axis: the deflection of the field lines in figure 2 is quite weak and the electric field only differs from its value at infinity in a thin layer near the surface of the spheroid. This comes from the fact that the geometry is three-dimensional and a significant azimuthal field exists when $\phi \neq 0$, so that the deflection of the field lines occurs on length scales of the order of the spheroid thickness $2a$. Equations (2.8)–(2.9) also show that the electric field disturbance decays quite rapidly as $1/|\boldsymbol{x}|^3$ (vs. $1/|\boldsymbol{x}|^2$ in two dimensions), and Taylor expansions of $\beta_{\parallel}$ and $\beta_{\perp}$ as $\alpha \to 0$ show that both of these coefficients scale as α^2:

$$\boldsymbol{E}(\boldsymbol{x}) - \boldsymbol{E}_{\infty} \sim E_{\infty} \alpha^2 \frac{l^3}{|\boldsymbol{x}|^3}. \qquad (2.16)$$
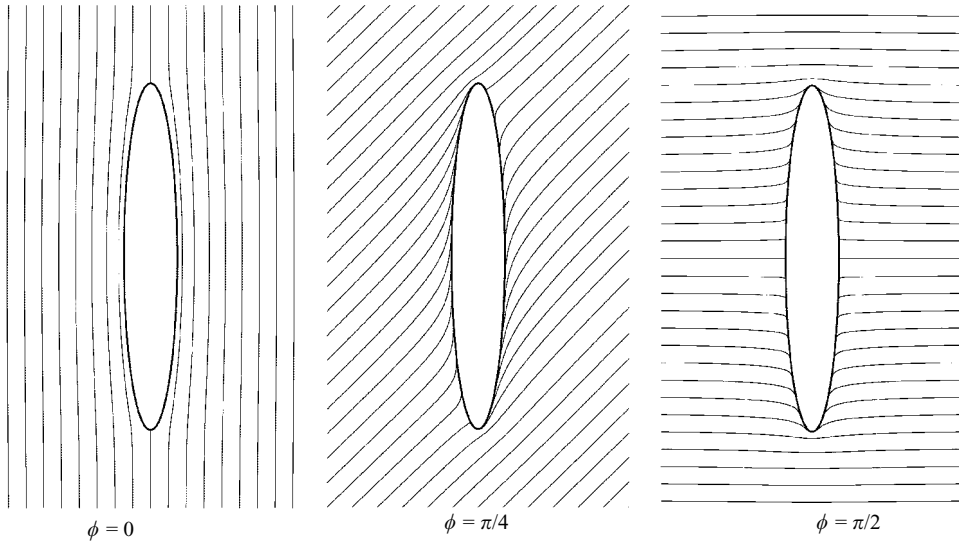
$\phi = 0$ $\phi = \pi/4$ $\phi = \pi/2$

FIGURE 2. Electric field lines, in the (x,z)-plane around a non-conducting spheroid of aspect ratio $\gamma = 6.5$ for various orientations ϕ of the electric field, calculated from equation (2.8). In three dimensions the deflection of the streamlines occurs over lengths scales of the order of the particle radius a, and the disturbance to the imposed field is very weak.

The perturbation to the imposed uniform electric field in the case of slender particles is therefore very weak, and we can safely expect electric interactions between particles in a dilute suspension to be negligible. This is to be contrasted with the flow disturbance due to induced-charge electrophoresis, which as we show in §2.2 decays more slowly as $1/|\boldsymbol{x}|^2$, and scales with the large dimension $2l$ of the particle.

2.1.2. *Slip velocity and flow problem*

The electric potential at the outer edge of the electrical double layer is equivalent to an induced zeta-potential, which varies along the surface of the particle and scales linearly with the imposed field. Following Squires & Bazant (2004, 2006), we can write the total zeta-potential on the surface as

$$\zeta(\boldsymbol{x}) = \Phi_0 - \Phi_s(\boldsymbol{x}) = \Phi_0 + \boldsymbol{x} \cdot \mathsf{G} \cdot \boldsymbol{E}_\infty \qquad \text{for } \boldsymbol{x} \in \partial S, \qquad (2.17)$$

where the constant potential Φ_0 is determined to ensure that the area average of $\zeta(\boldsymbol{x})$ yields the native zeta-potential ζ_0 of the particle surface, which is assumed to be uniform:

$$\frac{1}{S} \int_{\partial S} \zeta(\boldsymbol{x}) \, \mathrm{d}S = \zeta_0, \quad \text{i.e.} \quad \Phi_0 = \zeta_0 + \frac{1}{S} \int_{\partial S} \Phi_s(\boldsymbol{x}) \, \mathrm{d}S, \qquad (2.18)$$

where S denotes the surface area of the spheroid. Note that for the surface potential equation (2.13) determined in §2.1.1, the constant potential Φ_0 is simply the native zeta-potential: $\Phi_0 = \zeta_0$. The non-uniform zeta-potential equation (2.17), along with the expression for the tangential component of the electric field (equation 2.13), can be substituted into the Helmholtz–Smoluchowski equation (1.1) for the electrophoretic slip velocity on the surface of the particle, yielding

$$\boldsymbol{u}_s(\boldsymbol{x}) = -\frac{\varepsilon \zeta}{\mu} \boldsymbol{E}_s = -\frac{\varepsilon}{\mu} (\zeta_0 + \boldsymbol{x} \cdot \mathsf{G} \cdot \boldsymbol{E}_\infty) \times [(\boldsymbol{I} - \boldsymbol{nn}) \cdot \mathsf{G} \cdot \boldsymbol{E}_\infty]. \qquad (2.19)$$

This slip velocity contains a linear contribution $-\varepsilon\zeta_0 \boldsymbol{E}_s/\mu$, which is due to the native zeta-potential and corresponds to classical electrophoresis (Fair & Anderson 1989), and a quadratic contribution $-\varepsilon(\boldsymbol{x}\cdot\boldsymbol{G}\cdot\boldsymbol{E}_\infty)\boldsymbol{E}_s/\mu$, which is induced by the polarization and is responsible for induced-charge electrophoresis.

Fair & Anderson (1989) made use of the Lorentz reciprocal theorem to derive the linear and angular velocities of a spheroid undergoing phoretic motion in Stokes flow with an arbitrary slip velocity:

$$\boldsymbol{U} = -(3V_p)^{-1}\iint_{\partial S}(\boldsymbol{n}\cdot\boldsymbol{x})\boldsymbol{v}_s(\boldsymbol{x})\,\mathrm{d}S, \tag{2.20}$$

$$\boldsymbol{\Omega} = -(2V_p)^{-1}\left[l^{-2}\boldsymbol{pp} + (a^2+l^2)^{-1}(\boldsymbol{I}-\boldsymbol{pp})\right]\cdot\iint_{\partial S}(\boldsymbol{n}\cdot\boldsymbol{x})\boldsymbol{x}\times\boldsymbol{v}_s(\boldsymbol{x})\,\mathrm{d}S, \tag{2.21}$$

where $V_p = 4\pi l a^2/3$ is the volume of the spheroid. Equations (2.20)–(2.21) are a special case of the more general expressions found by Yariv (2005). It can be shown that the linear part of the slip velocity leads to translation of the particle without rotation as in classical electrophoresis, while the quadratic part does not cause translation but results in a rotation that tends to align the particle in the direction of the electric field. As noted by Bazant & Squires (2004), Yariv (2005), and Squires & Bazant (2006), the absence of a translational induced-charge electrophoretic velocity is a consequence of the fore–aft symmetry of the particle: an asymmetric particle would feel a quadratic translational velocity that, quite interestingly, would not change sign upon reversal of the electric field. In the remainder of the paper we will focus on the induced-charge effects and therefore discard the linear term in the slip velocity ($\zeta_0 \equiv 0$), as it has been studied extensively in the past (e.g. Fair & Anderson 1989; Solomentsev & Anderson 1994).

In addition to causing rotation, the slip velocity also drives a disturbance flow in the surrounding fluid. The induced velocity can be obtained as a solution of the Stokes equations:

$$-\mu\nabla^2\boldsymbol{u} + \nabla p = \boldsymbol{0}, \quad \nabla\cdot\boldsymbol{u} = 0, \tag{2.22}$$

subject to the boundary conditions:

$$\left.\begin{aligned}\boldsymbol{u}(\boldsymbol{x}) &= \boldsymbol{U} + \boldsymbol{\Omega}\times\boldsymbol{x} + \boldsymbol{u}_s(\boldsymbol{x}) && \text{as } \boldsymbol{x}\in\partial S,\\\boldsymbol{u}(\boldsymbol{x}) &\rightarrow \boldsymbol{0} && \text{as } |\boldsymbol{x}|\rightarrow\infty.\end{aligned}\right\} \tag{2.23}$$

Once again, the slip boundary condition in equation (2.23) applies at the outer edge of the electrical double layer, but can be enforced on the particle surface in the thin EDL limit. Except in a few special cases such as a perfect sphere or an infinite cylinder (Squires & Bazant 2004) as well as slightly deformed spheres (Squires & Bazant 2006), the complexity of the slip velocity equation (2.19), which depends on both coordinates z and θ on the surface of the particle, precludes one from solving equations (2.22)–(2.23) analytically. Numerical solutions could be obtained using boundary integral methods, such as that described by Youngren & Acrivos (1975), which are easily modified to allow a slip boundary condition. Such methods however are costly and would only allow the calculation of the flow around a few particles. As we show in the next section, the case of high-aspect-ratio particles ($\gamma = \alpha^{-1} \gg 1$) is amenable to an approximate solution based on slender-body theory.

2.2. *Slender-body formulation*

Slender-body theory for Stokes flow approximates the velocity disturbance induced by a particle whose length is much greater than its radius by a line distribution of

point-force singularities along the particle axis. It was first introduced by Batchelor (1970) and Cox (1970) for a rigid axisymmetric particle in a prescribed flow field. Its application to electrophoresis was described by Solomentsev & Anderson (1994); recently Sellier (2000) considered the more general case of a body of non-uniform zeta-potential and non-circular cross-section in an axisymmetric electric field. Batchelor's result, modified to include a slip boundary condition on the particle surface by Solomentsev & Anderson (1994), relates the linear and angular velocities of the particle to the imposed fluid velocity u' (which may include the velocity disturbance in the fluid due to other particles), slip velocity u_s, and line distribution of point forces $f(s)$ in the following way:

$$U + s\boldsymbol{\Omega} \times \boldsymbol{p} + \tilde{\boldsymbol{u}}_s(s) - \boldsymbol{u}'(\boldsymbol{x} + s\boldsymbol{p}) = \frac{\log 2\gamma}{4\pi\mu}(\boldsymbol{I} + \boldsymbol{pp}) \cdot \boldsymbol{f}(s) + O(|\boldsymbol{f}|/\mu), \quad (2.24)$$

where x denotes the position of the particle centre of mass, and where we introduced the circumferential average $\tilde{u}_s(s)$ of the slip velocity (Solomentsev & Anderson 1994):

$$\tilde{\boldsymbol{u}}_s(s) = \frac{1}{2\pi} \int_0^{2\pi} \boldsymbol{u}_s(s, \theta) \, \mathrm{d}\theta. \quad (2.25)$$

Note that this model, which describes the disturbance flow around the particle as that induced by a line distribution of point forces only, neglects the effects of particle thickness on the flow, and is therefore only valid for very slender particles. To account for the thickness of the particle, distributions of higher-order singularities (typically potential dipoles), would have to be included in the formulation, as previously done for instance by Claeys & Brady (1993) in their Stokesian dynamics simulations of rigid spheroids. These additional singularities however would all contribute to higher-order terms in the slender-body equation (2.24).

The linear and angular velocities of the particle can then be obtained by integration of equation (2.24):

$$U = \frac{1}{2l} \int_{-l}^{l} [\boldsymbol{u}'(\boldsymbol{x} + s\boldsymbol{p}) - \tilde{\boldsymbol{u}}_s(s)] \, \mathrm{d}s + \frac{\log 2\gamma}{8\pi\mu l}(\boldsymbol{I} + \boldsymbol{pp}) \cdot \boldsymbol{F}, \quad (2.26)$$

$$\boldsymbol{\Omega} = \frac{3}{2l^3} \int_{-l}^{l} s\boldsymbol{p} \times [\boldsymbol{u}'(\boldsymbol{x} + s\boldsymbol{p}) - \tilde{\boldsymbol{u}}_s(s)] \, \mathrm{d}s + \frac{3\log 2\gamma}{8\pi\mu l^3}\boldsymbol{T}. \quad (2.27)$$

Here F and T denote the external force and torque on the particle:

$$\boldsymbol{F} = \int_{-l}^{l} \boldsymbol{f}(s) \mathrm{d}s, \quad \boldsymbol{T} = \int_{-l}^{l} s\boldsymbol{p} \times \boldsymbol{f}(s) \, \mathrm{d}s. \quad (2.28)$$

In particular we will show below that the interaction of the induced dipole of the rod with the applied field results in an electric torque on the particle, calculated in §2.4.

In addition to yielding simple expressions for the motion of the particle, this slender-body formulation also allows an easy calculation of the disturbance flow induced by the particle. Indeed, the disturbance flow is that created by the line distribution of point forces $f(s)$, which is known from inverting equation (2.24):

$$\boldsymbol{f}(s) = \frac{4\pi\mu}{\log 2\gamma} \left(\boldsymbol{I} - \frac{1}{2}\boldsymbol{pp}\right) \cdot [U + s\boldsymbol{\Omega} \times \boldsymbol{p} + \tilde{\boldsymbol{u}}_s(s) - \boldsymbol{u}'(\boldsymbol{x} + s\boldsymbol{p})]. \quad (2.29)$$

Equation (2.29), along with equations (2.26)–(2.27), entirely determines $f(s)$ provided that the external force and torque on the particle, the imposed flow velocity, and the
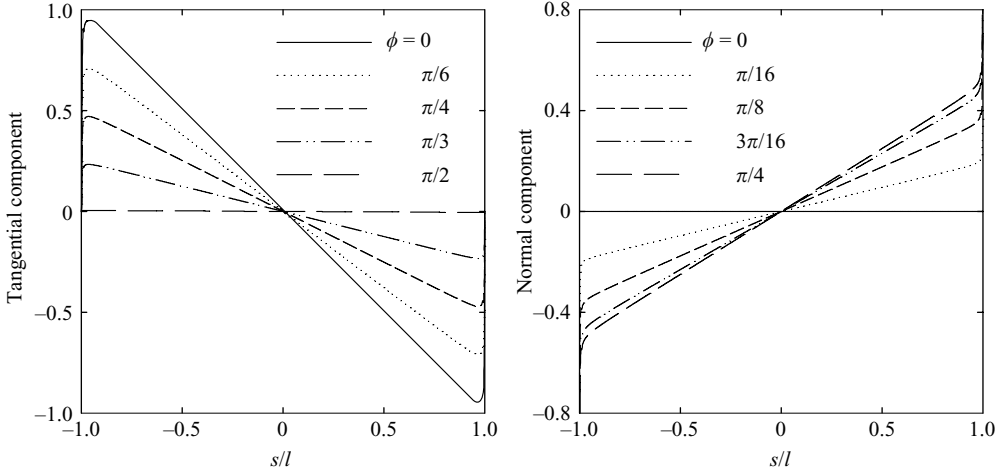
FIGURE 3. Tangential and normal components (with respect to the orientation vector $\boldsymbol{p}$) of the dimensionless circumferentially averaged slip velocity $\tilde{\boldsymbol{u}}_s(s)/(\varepsilon E_\infty^2/\mu)$, for various orientations ϕ of the electric field.

circumferentially averaged slip velocity are known. The disturbance velocity field at a position $\boldsymbol{y}$ in the fluid is then obtained as a convolution:

$$\boldsymbol{u}'(\boldsymbol{y}) = \frac{1}{8\pi\mu} \int_{-l}^{l} \boldsymbol{K}(\boldsymbol{y}; \boldsymbol{x} + s\boldsymbol{p}) \cdot \boldsymbol{f}(s) \, \mathrm{d}s, \qquad (2.30)$$

where $\boldsymbol{K}$ is the appropriate Green's function for Stokes flow. For a particle suspended in an infinite fluid, $\boldsymbol{K}$ is the Oseen–Burgers tensor:

$$\boldsymbol{K}(\boldsymbol{y}; \boldsymbol{x}) = \boldsymbol{K}(\boldsymbol{y} - \boldsymbol{x}) = \frac{\boldsymbol{I}}{|\boldsymbol{y} - \boldsymbol{x}|} + \frac{(\boldsymbol{y} - \boldsymbol{x})(\boldsymbol{y} - \boldsymbol{x})}{|\boldsymbol{y} - \boldsymbol{x}|^3}. \qquad (2.31)$$

2.3. Slip velocity linearization

The previous discussion showed that the induced-charge electrophoretic motion of a slender body, along with the associated disturbance velocity field in the fluid, are entirely determined by the circumferentially averaged slip velocity $\tilde{\boldsymbol{u}}_s$, which can be obtained by averaging equation (2.19) over the azimuthal direction. Its tangential and normal components with respect to the orientation vector $\boldsymbol{p}$ are

$$\boldsymbol{p}\boldsymbol{p} \cdot \tilde{\boldsymbol{u}}_s(s) = -\frac{\varepsilon E_\infty^2}{\mu} s G_\parallel^2 \cos^2\phi \left[1 - \frac{2\alpha^2 s^2 + \alpha^2(1 - s^2)(G_\perp/G_\parallel)^2 \tan^2\phi}{2(1 - s^2 + \alpha^2 s^2)} \right] \hat{\boldsymbol{z}}, \quad (2.32)$$

$$(\boldsymbol{I} - \boldsymbol{p}\boldsymbol{p}) \cdot \tilde{\boldsymbol{u}}_s(s) = \frac{\varepsilon E_\infty^2}{\mu} s G_\perp G_\parallel \cos\phi \sin\phi \left[1 - \frac{(1 + \alpha^2)(1 - s^2)}{2(1 - s^2 + \alpha^2 s^2)} \right] \hat{\boldsymbol{x}}. \qquad (2.33)$$

These components are plotted in dimensionless form in figure 3 for an aspect ratio of $\alpha^{-1} = 20$ and for various orientations ϕ of the electric field. Figure 3 shows that both components vary almost linearly along the axis of the particle, the only significant departure occurring near the ends. This is also confirmed by an expansion

of equations (2.32)–(2.33) as $\alpha \to 0$, and justifies the following linearization of the slip velocity for high-aspect-ratio particles:

$$\boldsymbol{pp} \cdot \tilde{\boldsymbol{u}}_s(s) \approx -\frac{\varepsilon E_\infty^2}{\mu} s G_\parallel^2 \cos^2 \phi \, \hat{\boldsymbol{z}}, \qquad (2.34)$$

$$(\boldsymbol{I} - \boldsymbol{pp}) \cdot \tilde{\boldsymbol{u}}_s(s) \approx \frac{\varepsilon E_\infty^2}{2\mu} s G_\perp G_\parallel \cos \phi \sin \phi \, \hat{\boldsymbol{x}}, \qquad (2.35)$$

where in each case the error in the linearization is of $O(\alpha^2)$. Equations (2.34)–(2.35) are conveniently recast in a frame-independent manner:

$$\tilde{\boldsymbol{u}}_s(s) \approx -\frac{\varepsilon}{\mu} s (\boldsymbol{p} \cdot \tilde{\boldsymbol{E}}_\infty) \tilde{\boldsymbol{E}}_\infty + O(\alpha^2), \qquad (2.36)$$

where we have introduced the following notation:

$$\tilde{\boldsymbol{E}}_\infty = \left[G_\parallel \boldsymbol{pp} + \tfrac{1}{2} G_\perp (\boldsymbol{I} - \boldsymbol{pp}) \right] \cdot \boldsymbol{E}_\infty. \qquad (2.37)$$

Note that in the limit of high aspect ratio ($\alpha^{-1} \gg 1$) we have $\tilde{\boldsymbol{E}}_\infty \approx \boldsymbol{E}_\infty$.

From the discussion of §2.2 on slender-body theory, we infer that the induced translational velocity is zero: $\boldsymbol{U}_s = \boldsymbol{0}$. The normal component of the slip contributes to an angular velocity:

$$\boldsymbol{\Omega}_s = \frac{\varepsilon}{\mu} \boldsymbol{p} \times \tilde{\boldsymbol{E}}_\infty (\boldsymbol{p} \cdot \tilde{\boldsymbol{E}}_\infty). \qquad (2.38)$$

The force distribution along the particle axis is linear and is given by

$$\boldsymbol{f}(s) = -\frac{2\pi\varepsilon s}{\log 2\gamma} \boldsymbol{p} (\boldsymbol{p} \cdot \tilde{\boldsymbol{E}}_\infty)^2. \qquad (2.39)$$

Equation (2.30) can then be used to evaluate the velocity disturbance in the fluid.

It is enlightening for the purpose of understanding hydrodynamic interactions between suspended particles to investigate the far-field behaviour of the velocity disturbance. The asymptotic behaviour as $|\boldsymbol{x}|/l \to \infty$ can be obtained by performing a multipole expansion about the centre of the particle, in which it is straightforward to see that the linear force distribution only contributes to the first force moment, termed force dipole (Kim & Karrila 1991). This was pointed out by Batchelor (1970), who observed that a linear force distribution on a slender body results in stresslet and rotlet flows in the far field. In the case of interest here, the rotlet flow is zero since induced-charge electrophoresis creates no torque and the force distribution equation (2.39) is tangential to the rod axis. The stresslet disturbance flow $\boldsymbol{u}_S'$ can be shown to be

$$\boldsymbol{u}_S'(\boldsymbol{x}) = -3 \frac{(\boldsymbol{x} \cdot \boldsymbol{S} \cdot \boldsymbol{x}) \boldsymbol{x}}{8\pi\mu |\boldsymbol{x}|^5}, \qquad (2.40)$$

where the second-order traceless tensor $\boldsymbol{S}$ is given by

$$\boldsymbol{S} = \frac{4\pi\varepsilon l^3}{3 \log 2\gamma} (\boldsymbol{p} \cdot \tilde{\boldsymbol{E}}_\infty)^2 \left(\boldsymbol{pp} - \frac{\boldsymbol{I}}{3} \right). \qquad (2.41)$$

An important conclusion of this analysis is the far-field decay as $1/|\boldsymbol{x}|^2$ and scaling with $(\log 2\gamma)^{-1}$ of the velocity disturbance, as shown by equations (2.40)–(2.41). In particular, this can be compared to the decay of the electric field perturbation as $1/|\boldsymbol{x}|^3$, which furthermore scales with γ^{-2} (§2.1.1): this remark will justify neglecting

electric interactions between particles compared to hydrodynamic interactions in the subsequent discussion. Note that electric interactions may still become significant when two particles get very close to one another. In that case electric field gradients may indeed result in dielectrophoretic effects, which are not included in the present discussion: additional work will be required to determine the precise importance of these effects.

2.4. Electrorotational torque

In addition to the angular velocity $\boldsymbol{\Omega}_s$ induced by the slip velocity on the particle surface, rotation also occurs as a result of the interaction between the applied electric field and the dipole moment of the disturbance potential $\Phi(\boldsymbol{x}) - \Phi_\infty$, which creates an electrorotational torque (e.g. Jones & Washizu 1996; Han & Yang 1996; Squires & Bazant 2006). More precisely, a multipole expansion of the disturbance potential around the centre of the rod can be written as

$$\Phi(\boldsymbol{x}) + \boldsymbol{E}_\infty \cdot \boldsymbol{x} \approx \frac{1}{4\pi\varepsilon} \frac{\boldsymbol{d} \cdot \boldsymbol{x}}{|\boldsymbol{x}|^3} + \dots \qquad (2.42)$$

where the dipole strength $\boldsymbol{d}$ is easily obtained from equation (2.8) as

$$\boldsymbol{d} = -4\pi\varepsilon \int_{-c}^{c} (c^2 - s^2)(\beta_\parallel \hat{\boldsymbol{z}}\hat{\boldsymbol{z}} + \beta_\perp \hat{\boldsymbol{x}}\hat{\boldsymbol{x}}) \cdot \boldsymbol{E}_\infty \, \mathrm{d}s = \frac{8}{3}\pi\varepsilon l^3 \alpha^2 \tilde{\boldsymbol{E}}_\infty. \qquad (2.43)$$

A similar expression was previously obtained by Han & Yang (1996). The dipole moment $\boldsymbol{d}$ results in an electrorotational torque on the rod given by $\boldsymbol{T}_e = \boldsymbol{d} \times \boldsymbol{E}_\infty$, and yields the following angular velocity:

$$\boldsymbol{\Omega}_e = \frac{3\log 2\gamma}{8\pi\mu l^3} \boldsymbol{T}_e = \frac{\varepsilon \log 2\gamma}{\mu\gamma^2} \tilde{\boldsymbol{E}}_\infty \times \boldsymbol{E}_\infty, \qquad (2.44)$$

which also contributes to the alignment of the rod in the direction of the field. Note however that this angular velocity is weaker than that induced by the slip velocity (equation (2.38)) by a factor of $\log 2\gamma/\gamma^2 \approx 0.01$ for $\gamma = 20$. The electrorotational torque $\boldsymbol{T}_e$, which could easily be carried along, will therefore be neglected in the remainder of the paper.

3. Pair interactions

Substantial information about the macroscopic behaviour of a suspension can be obtained by a detailed understanding of pair interactions. In the following we use the results of the single-particle model of §2 to derive expressions for the relative motion between two rods undergoing induced-charge electrophoresis. A detailed model based on interactions between slender bodies is used to calculate the relative velocity in §3.1; asymptotic expressions for this velocity are also obtained in Appendix A by the method of reflections (Kim & Karrila 1991). We then apply the results of §3.1 to evaluate the pair distribution function in a dilute suspension of aligned rods in §3.2.

3.1. Relative velocity

As depicted in figure 4, we consider two rod-like particles, which for simplicity we take to be aligned in the direction of the electric field: $\boldsymbol{p}_1 = \boldsymbol{p}_2 = \boldsymbol{p}$. This assumption is reasonable as we showed that the electric field causes the particles to reorient; even in Brownian suspensions good alignment can be observed at sufficiently high Péclet number (§5.2.1). Let $\boldsymbol{x} = \boldsymbol{x}_2 - \boldsymbol{x}_1$ be the separation vector between the particle
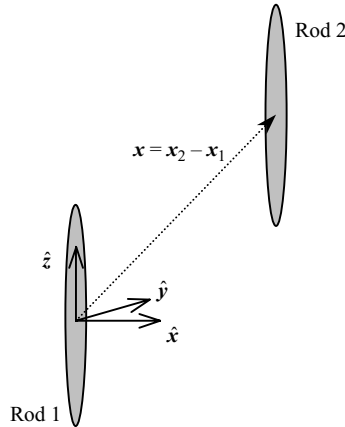
FIGURE 4. Particle pair considered in the analytical model of §3. For simplicity, the two rods are assumed to remain parallel and aligned in the direction of the electric field.

centres: we wish to determine the relative velocity $U = \dot{x}$ as a function of x. In this problem the particles, which are assumed to be aligned with the field, are force-free and torque-free (although this will be further discussed below): their only motion is therefore due to the velocity disturbance in the fluid, which is determined by the force distributions along the particle axes (equation (2.30)). Following the original idea of Harlen, Sundararajakumar & Koch (1999), we make the simplifying assumption that the force distributions can be linearized. This linearization was previously applied with success to study the sedimentation of rod-like particles (Butler & Shaqfeh 2002; Saintillan, Darve & Shaqfeh 2005), and is appropriate in this case as the slip velocities are themselves linear. For a force- and torque-free rod, the linear distribution is simply given by

$$f_\alpha(s_\alpha) = \frac{3}{2l^3} s_\alpha \mathscr{S}_\alpha p, \tag{3.1}$$

where $\alpha = 1, 2$. The scalar quantity $\mathscr{S}_\alpha$ is closely related to the magnitude of the tensor $\boldsymbol{S}$ introduced previously (equation (2.41)), and will therefore also be called a stresslet. It can be shown to be (Butler & Shaqfeh 2002)

$$\mathscr{S}_\alpha = -\frac{2\pi\mu}{\log 2\gamma} \int_{-l}^{l} s_\alpha p \cdot [u'_\alpha(x_\alpha + s_\alpha p) - \tilde{u}^s_\alpha(s_\alpha)] \, ds_\alpha, \tag{3.2}$$

where u'_α is the velocity disturbance created by the force distribution of rod $\beta \neq \alpha$. Recognizing that $\tilde{u}^s_\alpha$ and u'_α are given by equations (2.36) and (2.30) respectively, an equation can be derived that relates the two stresslets $\mathscr{S}_\alpha$ and $\mathscr{S}_\beta$:

$$\mathscr{S}_\alpha = -\frac{4\pi\varepsilon l^3}{3\log 2\gamma} G_\parallel^2 E_\infty^2 - \frac{3\mathscr{S}_\beta}{8l^3 \log 2\gamma} \iint_{-l}^{l} p \cdot \boldsymbol{K}(x + (s_\alpha - s_\beta)p) \cdot p s_\alpha s_\beta \, ds_\alpha \, ds_\alpha, \tag{3.3}$$

where $\boldsymbol{K}$ is again the Oseen–Burgers tensor (equation (2.31)). The first term on the right-hand side of equation (3.3) is created by the slip velocity on rod α, and is to be compared to equation (2.41). The second term however, which is linear in $\mathscr{S}_\beta$, is an induced stresslet which captures the effects of infinite reflections between the two rods. By symmetry it is possible to see that the two stresslets are equal: $\mathscr{S}_\alpha = \mathscr{S}_\beta = \mathscr{S}$;
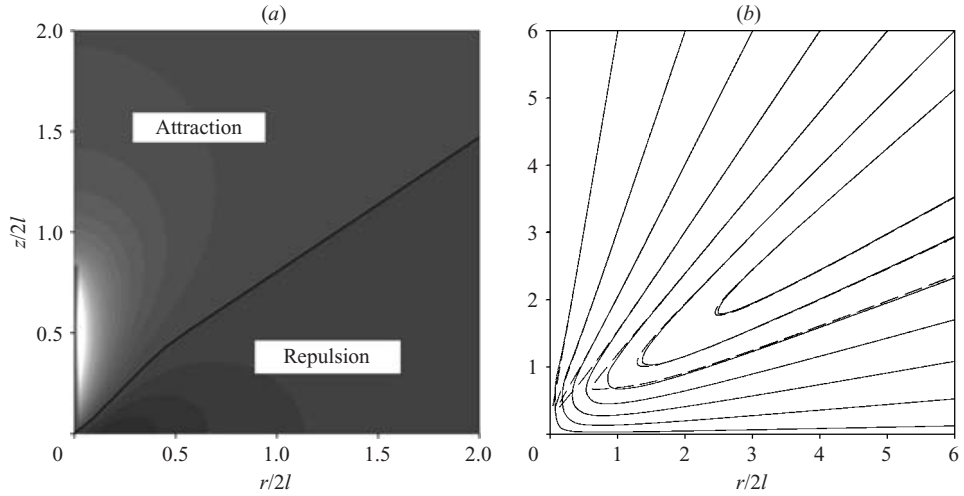
FIGURE 5. (a) Contours of the relative velocity magnitude $\dot{x} = (U \cdot x)/|x|$ between two parallel rods of aspect ratio $\gamma = 20$. The interaction between the particles transitions from being repulsive (dark grey) to attractive (light grey to white) when the direction of the separation vector x changes from perpendicular to parallel to the electric field; the neutral line where $\dot{x} = 0$ is drawn in black. The strongest attraction (white) occurs when the two rods are side by side with an offset of about half a particle length. (b) Relative trajectories in the reference frame of one of the two rods, calculated using the slender-body formulation of equation (3.5) (full lines), and using the method of reflections as shown in Appendix A (equation (A 17), dashed lines). Both methods yield indistinguishable results outside of a radius of approximately three rod lengths, but the asymptotic result fails at shorter distances.

they can be easily obtained from equation (3.3) as

$$\mathcal{S} = -\frac{32\pi\varepsilon G_{\parallel}^2 E_{\infty}^2 l^3}{24\log 2\gamma + 9H}, \quad \text{with} \quad H = \frac{1}{l^3} \iint_{-l}^{l} p \cdot K(x + (s_2 - s_1)p) \cdot p s_1 s_2 \, \mathrm{d}s_1 \, \mathrm{d}s_2. \quad (3.4)$$

Equations (2.26) and (2.30) then yield the relative velocity:

$$U = \dot{x}_2 - \dot{x}_1 = \frac{3\mathcal{S}}{16\pi\mu l^4} \iint_{-l}^{l} K(x + (s_2 - s_1)p) \cdot p s_1 \, \mathrm{d}s_1 \, \mathrm{d}s_2. \quad (3.5)$$

This expression is to be compared to the asymptotic result derived by the method of reflections and by multipole expansions in Appendix A. Using equations (3.4) and (3.5), in which the double integrals can be evaluated numerically, we calculated the relative velocity U for various separation vectors x. The results are summarized in figure 5(a), which shows contours of $\dot{x} = (U \cdot x)/|x|$ in the plane containing the two rods. In particular, we observe that depending on the separation vector the rods are either attracted or repelled. For separation vectors x that form an angle of less than approximately 55° with the electric field, attraction is observed, while repulsion occurs for other orientations. The strongest attraction, as indicated by the white region, occurs when the two rods are side by side and offset by about half a particle length. The presence of distinct regions of attraction and repulsion suggest that pairing may occur: this will be confirmed in the next section where we calculate the pair distribution function in a dilute suspension, as well as in the more detailed simulations that we describe in §4 and §5. Figure 5(b) also shows relative trajectories in the reference frame of one of the two rods, calculated using both equation (3.5)

and the far-field approximation obtained in Appendix A by the method of reflections (equation (A 17)). In particular, a comparison of the two methods shows that the method of reflections provides accurate results outside a radius of approximately three rod lengths, but fails at closer distances.

A few comments on the limitations of our model are in order. The two assumptions that the rods are both torque-free and aligned in the direction of the field are rigorously incompatible: hydrodynamic interactions indeed would cause slight rotations even in the presence of the electric field (see Appendix A), that could only be prevented by application of an external torque. However, departures from the exact alignment are typically very weak even when the rods are nearby (see figure 11(*d*) for instance), so that the error incurred by either neglecting rotations or neglecting the torque required to keep the rods aligned can be expected to be small. Other effects that have been left out and may play a role are close particle interactions such as excluded volume and lubrication: these are likely to influence velocities and trajectories in the near field, and will be accounted for in §4 and §5.

3.2. *Pair distribution function*

Our knowledge of the relative velocity between two rods (equation (3.5)) can be used to evaluate the pair distribution function in a dilute suspension. In the dilute regime pair interactions are most frequent, so that following Batchelor & Green (1972) we can define $P(\boldsymbol{x}_0 + \boldsymbol{x} \,|\, \boldsymbol{x}_0; t)$ as the probability density function at time t for finding a rod at position $\boldsymbol{x}_0 + \boldsymbol{x}$ knowing that a rod is located in $\boldsymbol{x}_0$, where once again all rods are assumed to remain aligned in the direction of the field. Outside the region of excluded volume, P can be normalized as

$$P(\boldsymbol{x}_0 + \boldsymbol{x} \,|\, \boldsymbol{x}_0; t) = np(\boldsymbol{x}/2l; t), \qquad (3.6)$$

where n is the number density in the suspension, and p tends to 1 as $|\boldsymbol{x}|/2l \to \infty$. In the absence of Brownian motion, p satisfies the following conservation equation:

$$\frac{\partial p}{\partial t} + \nabla \cdot (\boldsymbol{U}p) = 0, \qquad (3.7)$$

which at steady state reduces to

$$\boldsymbol{U} \cdot \nabla(\log p) = -\nabla \cdot \boldsymbol{U}. \qquad (3.8)$$

In equations (3.7) and (3.8), $\boldsymbol{U}$ is the relative velocity between two rods separated by $\boldsymbol{x}$, and is given by equation (3.5). In particular, the expression found for $\boldsymbol{U}$ has a non-zero divergence:

$$\nabla \cdot \boldsymbol{U} = \frac{3}{16\pi\mu l^4} \nabla \mathscr{S} \cdot \iint_{-l}^{l} \boldsymbol{K}(\boldsymbol{x} + (s_2 - s_1)\boldsymbol{p}) \cdot \boldsymbol{p} s_1 \, \mathrm{d}s_1 \, \mathrm{d}s_2 \neq 0, \qquad (3.9)$$

which is a consequence of accounting for multiple reflections between the two rods in equation (3.3). Integrating equation (3.8) analytically is not tractable in general, although we show in Appendix B that an asymptotic solution can be obtained in the far field. However the method of characteristics can be employed to obtain a numerical solution, by simultaneously integrating the two following equations:

$$\frac{\mathrm{d}\boldsymbol{x}}{\mathrm{d}t} = \boldsymbol{U}(\boldsymbol{x}), \qquad (3.10)$$

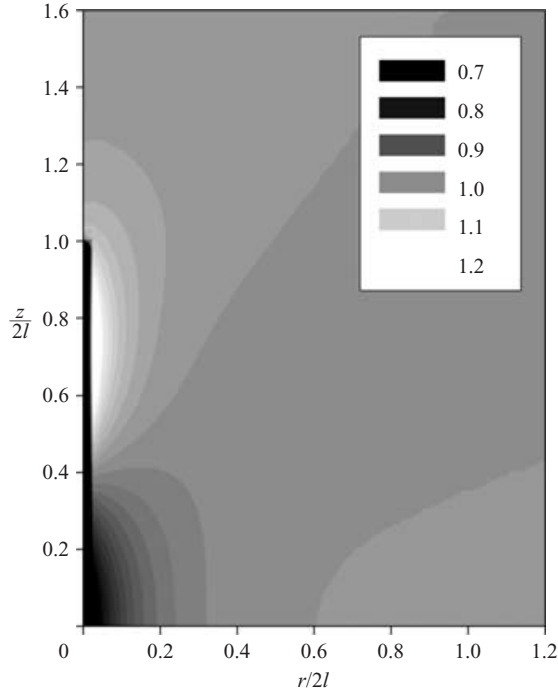$$\frac{\mathrm{d}}{\mathrm{d}t}(\log p) = -\nabla \cdot \boldsymbol{U}(\boldsymbol{x}), \qquad (3.11)$$

FIGURE 6. Pair distribution function $p(r/2l, z/2l)$ in a dilute suspension of rods of aspect ratio $\gamma = 20$, obtained by numerically solving the conservation equation (3.8) using the method of characteristics (equations (3.10)–(3.11)). The distribution function is normalized so that it tends to 1 far from the origin. The value of p was set to zero along the segment [0, 1] of the z-axis to reproduce the effects of excluded volume.

subject to the boundary condition $p(\boldsymbol{x}) \rightarrow 1$ as $|\boldsymbol{x}| \rightarrow \infty$. These equations were integrated numerically using a fourth-order Runge–Kutta time-marching scheme, along with a 50-point Gauss–Legendre quadrature for the double integrals in the expressions for the velocity. The results for rods of aspect ratio $\gamma = 20$ are shown in figure 6, in which the value of p was set to zero along the segment [0, 1] of the z-axis to reproduce the effects of excluded volume. The pair distribution of figure 6 presents several interesting features. In particular the presence of a sharp peak (white region) shows that there is a high probability of finding two particles next to one another, with an offset of slightly more than half a rod length, i.e. that particle pairings can be expected in a suspension. Conversely, the black region near the origin corresponds to a depletion, and suggests that it is highly unlikely for two particles to remain aligned side by side, as could have been expected from the relative velocity field of figure 5. Once again, the pair distribution of figure 6 can only be taken as qualitative owing to the limitations mentioned above; in particular close particle interactions will affect the shapes of the pairing and depletion regions as shown in §5.

4. Simulation method

In this section we describe a method for the simulation of high-aspect-ratio rod-like particles undergoing induced-charge electrophoresis, which includes both far-field hydrodynamic interactions and near-field lubrication forces, as well as Brownian motion. The method, which can be viewed as an extension of the two-particle model

of §3 to larger assemblies of particles, is based on the work of Butler & Shaqfeh (2002) for non-Brownian fibre suspensions, and is accelerated using the smooth particle-mesh Ewald algorithm described by Saintillan *et al.* (2005). Brownian motion is included in a self-consistent manner using a spectral approximation of the mobility square-root first suggested by Fixman (1986), in a similar way as was done in Stokesian dynamics simulations by Banchio & Brady (2003).

4.1. *Mathematical formulation*

4.1.1. *Equations of motion*

We consider a periodic system of N rods of aspect ratio γ in a box of dimensions $L_x \times L_y \times L_z$. We denote by $\boldsymbol{x}_\alpha$ and $\boldsymbol{p}_\alpha$ the position and orientation vectors of a given rod $\alpha = 1, \ldots, N$. Equations of motion for $\boldsymbol{x}_\alpha$ and $\boldsymbol{p}_\alpha$ are obtained from the slender-body formulation of §2.2:

$$\dot{\boldsymbol{x}}_\alpha = \int_{-1/2}^{1/2} \boldsymbol{u}'_\alpha \, \mathrm{d}s_\alpha + (\boldsymbol{I} + \boldsymbol{p}_\alpha \boldsymbol{p}_\alpha) \cdot \boldsymbol{F}_\alpha^{(0)}, \tag{4.1}$$

$$\dot{\boldsymbol{p}}_\alpha = 12 \, (\boldsymbol{I} - \boldsymbol{p}_\alpha \boldsymbol{p}_\alpha) \cdot \int_{-1/2}^{1/2} s \left[\boldsymbol{u}'_\alpha - Pe \, \tilde{\boldsymbol{u}}_\alpha^s \right] \mathrm{d}s_\alpha + 12 \, (\boldsymbol{I} - \boldsymbol{p}_\alpha \boldsymbol{p}_\alpha) \cdot \boldsymbol{F}_\alpha^{(1)}, \tag{4.2}$$

where $\boldsymbol{F}_\alpha^{(0)}$ and $\boldsymbol{F}_\alpha^{(1)}$ denote the zeroth and first moments of the force distribution along the rod of interest, respectively. In particular, in equation (4.2) we have replaced the angular velocity $\boldsymbol{\Omega}_\alpha$ and the torque $\boldsymbol{T}_\alpha$ on the particle by the rate of change $\dot{\boldsymbol{p}}_\alpha$ of the orientation vector and by the first force moment $\boldsymbol{F}_\alpha^{(1)}$, which avoids complications from dealing with pseudo-vectors (Butler & Shaqfeh 2002, 2005):

$$\dot{\boldsymbol{p}}_\alpha = (\boldsymbol{I} - \boldsymbol{p}_\alpha \boldsymbol{p}_\alpha) \cdot (\boldsymbol{\Omega}_\alpha \times \boldsymbol{p}_\alpha), \qquad \boldsymbol{F}_\alpha^{(0)} = \int_{-1/2}^{1/2} s_\alpha \boldsymbol{f}_\alpha(s_\alpha) \, \mathrm{d}s_\alpha. \tag{4.3}$$

If needed, $\boldsymbol{\Omega}_\alpha$ and $\boldsymbol{T}_\alpha$ can be obtained by the relations $\boldsymbol{\Omega}_\alpha = \boldsymbol{p}_\alpha \times \dot{\boldsymbol{p}}_\alpha$ and $\boldsymbol{T}_\alpha = \boldsymbol{p}_\alpha \times \boldsymbol{F}_\alpha^{(1)}$.

In this section and for all Brownian simulations, equations are made dimensionless by the following length, time and velocity scales:

$$l_c = 2l, \quad t_c = \frac{32\pi\mu l^3}{kT \log 2\gamma}, \quad u_c = \frac{l_c}{t_c} = \frac{kT \log 2\gamma}{16\pi\mu l^2}. \tag{4.4}$$

The thermal time scale t_c can be viewed as the characteristic time for a rod to diffuse over a distance equal to its length under the action of Brownian motion. In the case of non-Brownian systems discussed in §5.1, we shall use the electroviscous time, or characteristic time for fluid advection along the length of a rod under the action of the slip:

$$t_c = \frac{\mu}{\varepsilon E_\infty^2}, \quad u_c = \frac{l_c}{t_c} = \frac{2\varepsilon E_\infty^2 l}{\mu}. \tag{4.5}$$

The equations for the non-Brownian case can easily be obtained by setting the Brownian forces and torques to zero and changing the non-dimensionalization.

In equations (4.1)–(4.2), $\boldsymbol{u}'_\alpha$ is the velocity disturbance induced by rods $\beta \neq \alpha$ and evaluated at position $\boldsymbol{x}_\alpha + s_\alpha \boldsymbol{p}_\alpha$ along the rod axis; its calculation is explained in §4.1.2. The dimensionless slip velocity $\tilde{\boldsymbol{u}}_\alpha^s$ is obtained from equation (2.36) as

$$\tilde{\boldsymbol{u}}_\alpha^s(s_\alpha, \boldsymbol{p}_\alpha) = -s_\alpha(\boldsymbol{p}_\alpha \cdot \boldsymbol{e}_\alpha)\boldsymbol{e}_\alpha, \tag{4.6}$$

where e_α corresponds to $\tilde{E}_\infty$ after non-dimensionalization:

$$e_\alpha = \left[G_\| \, p_\alpha \, p_\alpha + \tfrac{1}{2} G_\perp (I - p_\alpha \, p_\alpha) \right] \cdot \hat{z}, \tag{4.7}$$

and where we have chosen the z-direction as the direction of the electric field. The strength of the electric field is captured by the Péclet number Pe in equation (4.2), which compares the magnitude of the slip velocity to the thermal velocity scale u_c:

$$Pe = \frac{2\varepsilon l E_\infty^2 / \mu}{u_c} = \frac{32\pi\varepsilon l^3 E_\infty^2}{kT \log 2\gamma}. \tag{4.8}$$

Neglecting the electrorotational torque as justified in §2.4, the external forces and torques on the rods will include contributions from Brownian motion, lubrication and contacts:

$$F_\alpha^{(0)} = F_\alpha^{(0),b} + F_\alpha^{(0),l} + F_\alpha^{(0),c}, \quad F_\alpha^{(1)} = F_\alpha^{(1),b} + F_\alpha^{(1),l} + F_\alpha^{(1),c}. \tag{4.9}$$

The Brownian forces and torques, which model thermal fluctuations of the solvent molecules, will be discussed in detail in §4.3. Lubrication interactions are short-range hydrodynamic interactions, which occur when two particle surfaces come close to contact (typically when the separation distance becomes of the order of a rod diameter). They can be calculated for various surface geometries using the theory by Claeys & Brady (1989); here we use the detailed formulae for spherocylinders given by Butler & Shaqfeh (2002). Note that these interactions are linear in the relative velocity between the two surfaces: their magnitudes are therefore indeterminate and must be solved for as part of the problem. Finally, contact forces are required to prevent overlap between the rods. We here follow the approach suggested by Durlofsky & Brady (1989), and model contacts by strong and short-ranged repulsive forces. The reader is referred to Butler & Shaqfeh (2002) and Saintillan *et al.* (2005) for more extensive discussions on both lubrication and contacts.

4.1.2. *Hydrodynamic interactions*

Hydrodynamic interactions between rods are captured through the disturbance velocity in equations (4.1)–(4.2), which is given by

$$u_\alpha'(x_\alpha + s_\alpha p_\alpha) = \frac{1}{2\log 2\gamma} \sum_{\beta=1}^{N} \int_{-1/2}^{1/2} J(x_\alpha + s_\alpha p_\alpha - x_\beta - s_\beta p_\beta) \cdot f_\beta(s_\beta) \, \mathrm{d}s_\beta. \tag{4.10}$$

The convolution kernel J is again the appropriate Green's function for Stokes flow. In §3, J was the Oseen–Burgers tensor K (equation (2.31)), which applies to a finite number of particles in an infinite fluid. Here we use the periodic Green's function K_p, which was derived by Hasimoto (1959) and accounts for periodic images in all three space dimensions. As a particle does not feel its own velocity disturbance, we subtract K from K_p in equation (4.10) when $\alpha = \beta$:

$$J(x_\alpha + s_\alpha p_\alpha - x_\beta - s_\beta p_\beta) = \begin{cases} K_p(x_\alpha + s_\alpha p_\alpha - x_\beta - s_\beta p_\beta) & \text{if } \alpha \neq \beta, \\ K_p(s_\alpha - s_\beta) - K(s_\alpha - s_\beta) & \text{if } \alpha = \beta. \end{cases} \tag{4.11}$$

When $\alpha = \beta$ and $s_\alpha = s_\beta$ the limit of $K_p(s_\alpha - s_\beta) - K(s_\alpha - s_\beta)$ is used.

Equations (4.1)–(4.2) and (4.10), along with the definition of the slip velocity and the force balance equation (4.9), define an integral system for the force distributions f_α along all the rods. Instead of solving for the exact force distributions by discretization of the rod axes (as was done for instance in the Monte-Carlo simulations of

Mackaplow & Shaqfeh 1998), we use the same approach as in the two-particle model of §3 and linearize the force distributions as follows:

$$\boldsymbol{f}_\alpha(s_\alpha) = \boldsymbol{F}_\alpha^{(0)} + 12\, s_\alpha \left[(\boldsymbol{I} - \boldsymbol{p}_\alpha \boldsymbol{p}_\alpha) \cdot \boldsymbol{F}_\alpha^{(1)} + \mathscr{S}_\alpha \boldsymbol{p}_\alpha \right], \tag{4.12}$$

in which the scalar stresslet $\mathscr{S}_\alpha$ is now defined in dimensionless form as

$$\mathscr{S}_\alpha = -\frac{1}{2} \int_{-1/2}^{1/2} s_\alpha\, \boldsymbol{p}_\alpha \cdot \left[\boldsymbol{u}'_\alpha - Pe\, \tilde{\boldsymbol{u}}_\alpha^s \right] \, \mathrm{d}s_\alpha. \tag{4.13}$$

The linearization of equation (4.12) corresponds to the first two terms in a spectral expansion of the force distribution using Legendre polynomials. Its level of approximation, as discussed by Butler & Shaqfeh (2002) and Saintillan *et al.* (2005), is equivalent to that of Stokesian dynamics simulations in which a multipole expansion is truncated after the dipole term (Brady & Bossis 1988).

The method of solution then proceeds as follows. Equations (4.6) and (4.10), when substituted into the definition of the stresslet equation (4.13), allow one to write a linear system for the stresslets $\mathscr{S}_\alpha(\alpha = 1, \ldots, N)$, and for the magnitudes of the lubrication forces. This linear system is inverted using a preconditioned generalized minimum-residual iterative method (see Saintillan *et al.* 2005). Once stresslets and lubrication forces are known, the dynamic equations (4.1)–(4.2) are used to integrate the position and orientation of the rod forward in time, using the midpoint algorithm of §4.4.

The calculation of the linear and angular velocities from the knowledge of the forces and torques on the particles corresponds to the so-called mobility problem (e.g. Brady & Bossis 1988). Let $\mathscr{U} = [\dot{\boldsymbol{x}}_\alpha, \ \dot{\boldsymbol{p}}_\alpha]^T$ denote the generalized velocity vector that contains the linear and angular velocities of all the rods, and $\mathscr{F} = [\boldsymbol{F}_\alpha^{(0)}, \ \boldsymbol{F}_\alpha^{(1)}]^T$ the generalized force vector that contains all the forces and torques of non-hydrodynamic nature (i.e. excluding lubrication). The method described above allows the calculation of $\mathscr{U}$ knowing $\mathscr{F}$, which we can write symbolically as (Butler & Shaqfeh 2005)

$$\mathscr{U} = \mathscr{U}^s + \mathscr{M} \cdot \mathscr{F}, \tag{4.14}$$

where $\mathscr{U}^s$ is induced by the electrophoretic slip velocity, and $\mathscr{M}$ is the grand mobility operator. This operator, which is a function of the particle configurations and solvent viscosity only, accounts for far-field hydrodynamics up to the stresslet term and for near-field lubrication. Note that the method described here does not explicitly compute the coefficients of matrix $\mathscr{M}$, but rather allows the efficient evaluation of the action of $\mathscr{M}$ on a given force vector $\mathscr{F}$.

4.2. *The smooth particle-mesh Ewald algorithm*

The direct calculation of the disturbance velocity along the length of each rod (equation (4.10)) is computationally intensive, with a quadratic cost in the number of particles. In a previous study we implemented a fast method called the smooth particle-mesh Ewald (SPME) algorithm, which reduces this cost to $O(N \log N)$ and thereby allows the simulation of much larger systems (Saintillan *et al.* 2005). The SPME algorithm, which is based on the Ewald summation formula of Hasimoto (1959) and on fast Fourier tranforms, has similarities with the accelerated Stokesian dynamics method of Sierou & Brady (2001). A brief outline of the method is given here, and the reader is referred to our original paper for more details.

Using numerical quadrature to evaluate line integrals, we can rewrite equation (4.10) as the velocity disturbance created by a discrete distribution of point forces

F_m ($m = 1, \ldots, M$) located at positions x_m:

$$u'(x_n) = \sum_{m=1}^{M} K_p(x_n - x_m) \cdot F_m, \qquad (4.15)$$

where K_p is the periodic Green's function for Stokes flow, from which the Oseen–Burgers tensor is subtracted if the two points x_n and x_m are on the same rod. As shown by Hasimoto (1959), such a sum can be recast into the Ewald summation formula:

$$u'(x_n) = \sum_{p} \sum_{m=1}^{M} A(\xi, x_n - x_m + p) \cdot F_m + \sum_{k \neq 0} \exp(-2\pi i k \cdot x_n) B(\xi, k) \cdot \hat{F}(k), \quad (4.16)$$

where the first sum is over all point forces F_m and their periodic images (as represented by the lattice vector p), and where the second sum over wavevectors k involves the Fourier transform of the force distribution:

$$\hat{F}(k) = \sum_{m=1}^{M} F_m \exp(2\pi i k \cdot x_m). \qquad (4.17)$$

The parameter ξ in equation (4.16), called Ewald coefficient, is user-defined and determines the relative importance of the two sums. The convolution kernels A and B are the following second-order tensors:

$$A(\xi, x) = \pi \xi^{-3/2} \phi_{1/2}(\pi \xi^{-1} |x|^2)(|x|^2 I + xx) - 2\xi^{-1/2} \exp(-\pi \xi^{-1} |x|^2) I, \qquad (4.18)$$

$$B(\xi, k) = \pi \xi^2 \tau^{-1} \phi_1(\pi \xi |k|^2)(|k|^2 I - kk), \qquad (4.19)$$

where τ is the volume of the unit periodic cell, and the functions ϕ_ν are incomplete Γ-functions:

$$\phi_{1/2}(x) = \frac{\exp(-x)}{x} + \frac{\mathrm{erfc}(\sqrt{x})}{2x}, \quad \phi_1(x) = \frac{\exp(-x)}{x^2}(1 + x). \qquad (4.20)$$

The major advantage of the Ewald summation formula equation (4.16) over the original convolution is that both tensors A and B now decay exponentially in their second argument. This very fast decay, together with the presence of Fourier transformations in the second sum, form the basis of the SPME algorithm. In SPME the Ewald coefficient ξ is chosen so as to make all the terms in the first sum (or real sum) negligible beyond a certain cutoff radius r_c. This allows truncation at a finite number of terms independent of the system size, so that the total cost of evaluating the real sum at all the particle locations scales linearly with the number of particles. For the second sum (or Fourier sum), the point-force distribution is assigned to a Cartesian grid by B-spline interpolation, and then transformed to Fourier space using the fast Fourier transform algorithm. The multiplication by the convolution kernel B is performed in Fourier space, and an inverse Fourier transform and an interpolation are applied to yield the value of the Fourier sum at the particle locations. The total cost of the method is determined by the fast Fourier transform, which scale as $O(K \log K)$, where K is the number of grid points and is chosen proportional to the number of particles; very good accuracy can be achieved by either increasing K or the interpolation order for the force assignment. A more thorough discussion of the accuracy and efficiency of the method can be found in Saintillan *et al.* (2005).

4.3. *Brownian forces: Fixman's method*

The Brownian forces and torques appearing in equation (4.9) are random variables that model the thermal collisions between the solvent molecules and the particles, and must be calculated to satisfy certain statistical properties (e.g. Butler & Shaqfeh 2005). Denoting by $\langle \cdot \rangle$ the ensemble average, we require in particular that the generalized Brownian force vector $\mathscr{F}^b$ have zero mean at any given time:

$$\langle \mathscr{F}^b(t) \rangle = 0, \tag{4.21}$$

and that its variance satisfy the fluctuation–dissipation theorem from statistical mechanics (e.g. Doi & Edwards 1986):

$$\langle \mathscr{F}^b(t) \otimes \mathscr{F}^b(t') \rangle = 2\,\delta(t - t')\,\mathscr{M}^{-1}, \tag{4.22}$$

where $\delta(t)$ is the Dirac delta function, and $\mathscr{M}$ is the grand mobility operator introduced in §4.1.2. The conditions (4.21)–(4.22) can be satisfied in a number of ways. In a computer simulation where time is discretized, the generalized Brownian force vector over a step of length Δt is typically calculated as (e.g. Bossis & Brady 1987)

$$\mathscr{F}^b = \sqrt{\frac{2}{\Delta t}}\,\mathscr{B} \cdot \mathscr{W}, \tag{4.23}$$

where the matrix $\mathscr{B}$ can be obtained as either the square root or the Cholesky decomposition of the inverse mobility: $\mathscr{B} \cdot \mathscr{B} = \mathscr{M}^{-1}$ or $\mathscr{B} \cdot \mathscr{B}^T = \mathscr{M}^{-1}$, and where $\mathscr{W}$ is a vector of length $6N$ containing random numbers from a Gaussian distribution with zero mean and unit variance.

Calculating the square root or the Cholesky decomposition of $\mathscr{M}^{-1}$, in addition to being computationally prohibitive with a cost of $O(N^3)$, also requires knowledge of the coefficients of the grand mobility. As discussed by Saintillan *et al.* (2005) and in §4.1.2, such knowledge cannot be obtained when using the SPME algorithm owing the fast Fourier transforms which circumvent the direct calculation of $\mathscr{M}$. A solution to this problem consists of using a spectral approximation of the matrix square root, based on Chebyshev polynomials. This method, termed Fixman's method after its first application to hydrodynamic interactions inside polymer chains by Fixman (1986), was more recently used in bead–spring simulations of polymers by Jendrejack, Graham & de Pablo (2000), and in Stokesian dynamics simulations of colloidal sphere dispersions by Banchio & Brady (2003). If we denote by $[\lambda_{\min}, \lambda_{\max}]$ the range of the eigenvalues of the grand mobility, we can find an approximation to the inverse square root valid over that range on the basis of Chebyshev polynomials:

$$x^{-1/2} \approx \sum_{i=1}^{n_p} a_i\,P_i(x). \tag{4.24}$$

The Chebyshev polynomials P_i are calculated by recursion:

$$P_0(\tilde{x}) = 1, \quad P_1(\tilde{x}) = \tilde{x}, \quad P_{i+1}(\tilde{x}) = 2\tilde{x}\,P_i(\tilde{x}) - P_{i-1}(\tilde{x}), \tag{4.25}$$

where $\tilde{x} \in [-1, 1]$ is a shifted coordinate:

$$\tilde{x} = \frac{2x}{\lambda_{\max} - \lambda_{\min}} - \frac{\lambda_{\max} + \lambda_{\min}}{\lambda_{\max} - \lambda_{\min}}. \tag{4.26}$$

The Chebyshev coefficients a_i, which decay exponentially, can be calculated using a fast cosine transform algorithm (Canuto *et al.* 1988). If equation (4.24) is uniformly valid over the range of the eigenvalues, by transformation to the basis of the

eigenvectors of $\mathcal{M}$ it is easy to see that the following approximation is also valid for the mobility:

$$\mathcal{B} \cdot \mathcal{W} = \mathcal{M}^{-1/2} \cdot \mathcal{W} \approx \sum_{i=1}^{n_p} a_i P_i(\mathcal{M}) \cdot \mathcal{W}, \tag{4.27}$$

for any vector $\mathcal{W}$. The evaluation of the right-hand side in equation (4.27) using the recursion formulae for the Chebyshev polynomials now only requires the action of the grand mobility operator on given vectors, and can therefore be performed with our algorithm.

As noted by Butler & Shaqfeh (2005), the grand mobility matrix defined in §4.1.2 is not positive definite: some of its eigenvalues can be shown to be zero owing to the restriction that the orientation vectors $\boldsymbol{p}_\alpha$ must remain normalized. This prevents the calculation of the inverse square root using the method described above, as no valid polynomial approximation to $x^{-1/2}$ can be found over an interval of the type $[0, \lambda_{\max}]$. Butler & Shaqfeh (2005) however noted that $\mathcal{M}$ can be decomposed as:

$$\mathcal{M} = \mathcal{K} \cdot \mathcal{M}' \cdot \mathcal{K}, \quad \text{with} \quad \mathcal{K} = \begin{bmatrix} \boldsymbol{I} & 0 \\ 0 & \boldsymbol{I} - \boldsymbol{p}_\alpha \boldsymbol{p}_\alpha \end{bmatrix}, \tag{4.28}$$

where each block in $\mathcal{K}$ has size $3N \times 3N$. In equation (4.28) the matrix $\mathcal{M}'$ is now positive definite, so that Fixman's method can be applied. A generalized Brownian force vector that satisfies the fluctuation–dissipation theorem is then constructed as follows:

$$\mathcal{F}^b = \sqrt{\frac{2}{\Delta t}} \mathcal{K} \cdot \mathcal{B}' \cdot \mathcal{W}, \quad \text{where} \quad \mathcal{B}' = (\mathcal{M}')^{-1/2}. \tag{4.29}$$

In our computer implementation we truncate the polynomial expansions so as to maintain an accuracy of approximately three significant figures. The range of the eigenvalues of the grand mobility, which determines the convergence of the expansions, is calculated using an iterative method. As its determination can be quite costly, the range is only updated when the particle configurations have changed significantly. Larger errors are sometimes tolerated when two particles become very close to one another, as lubrication interactions typically result in a very stiff grand mobility, for which the convergence of the expansion is slow.

4.4. *Time integration: midpoint algorithm*

As recommended by Grassia, Hinch & Nitsche (1995) for the integration of Langevin equations with configuration-dependent mobilities, we use the second-order midpoint algorithm of Fixman (1978) to advance particle configurations in time. If we let $\mathcal{R}_n = [\boldsymbol{x}_\alpha^n, \boldsymbol{p}_\alpha^n]^T$ denote the generalized configuration vector that contains all the rod positions and orientations at time t_n, the configuration $\mathcal{R}_{n+1}$ at time $t_{n+1} = t_n + \Delta t$ is obtained by a two-step procedure:

$$\mathcal{R}_* = \mathcal{R}_n + \tfrac{1}{2} \left[\mathcal{U}_n^s + \mathcal{M}_n \cdot \left(\mathcal{F}_n^c + \mathcal{F}_n^b \right) \right] \Delta t, \tag{4.30}$$

$$\mathcal{R}_{n+1} = \mathcal{R}_* + \left[\mathcal{U}_*^s + \mathcal{M}_* \cdot \left(\mathcal{F}_*^c + \mathcal{F}_n^b \right) \right] \Delta t, \tag{4.31}$$

where $\mathcal{U}^s$ is the generalized velocity vector containing the angular velocities from induced-charge electrophoresis (e.g. equation (4.2)), and where all hydrodynamic interactions (including lubrication) are contained in the grand mobility. Most importantly, the Brownian forces $\mathcal{F}^b$, which are obtained using the method discussed in §4.3, are not updated during the second step (equation (4.31)): this allows the drift term $(\nabla \cdot \mathcal{M})\Delta t$ that arises in Langevin equations with configuration-dependent

mobilities to be reproduced, and which one would need to include explicitly in a first-order integration scheme (Ermak & McCammon 1978; Fixman 1978; Grassia *et al.* 1995).

5. Results and discussion

We start by describing results for non-Brownian suspensions (infinite Péclet number limit) in §5.1, in which the effects of induced-charge electrophoresis on the dynamics can be isolated; Brownian motion is then discussed in §5.2. The non-Brownian results were typically obtained in suspensions of 400 rods, whereas smaller systems of 60 to 100 rods were used in the Brownian case. In all simulations 8 quadrature points were used along the rod lengths.

5.1. *Infinite Péclet number*

5.1.1. *Particle distributions and pair probabilities*

A typical particle distribution at infinite Péclet number is shown in figure 11(*d*) at steady state, where we see that all particles are very well aligned in the direction of the electric field (z-direction). This alignment occurs rapidly as soon as the field is turned on, and remains very strong, with some fluctuations occurring as a result of particle–particle interactions. These fluctuations are more frequent in more concentrated suspensions, but for all concentrations investigated the second moment $\langle p_z p_z \rangle$ of the z-component of the orientation vector typically remained above 0.99.

Once the particles are aligned, hydrodynamic interactions result in relative motions with no net velocity, which lead to a subtle rearrangement of the particle distributions. In particular, snapshots of the suspensions show the presence of particle pairs, which would be unlikely in a random suspension. More precisely, these pairing events consist of the following steps: two particles are attracted from their ends, slide along one another until they become side by side, then separate in the lateral direction. These dynamics confirm the analysis of pair interactions carried out in §3, where we identified regions of attraction and repulsion.

While these pairing events are typically ephemeral, they are frequent enough to modify the pair distribution function in the suspension. This is illustrated in figure 7, which shows the pair distribution function $p(r, z)$ (in cylindrical coordinates) at two effective volume fractions nl^3 (where n is the number density and l the rod half-length), where p is normalized so that it tends towards 1 at infinity. Figure 7 can be compared to figure 6, which had been obtained by numerically solving the conservation equation for the pair probabilities. While the two figures differ in details, the qualitative features are similar. The region of excluded volume is located along the z-axis since the rods are aligned in the direction of the electric field, and is coloured in black in figure 7. As expected its length is approximately one rod length, and its width is of the order of a rod diameter (in fact slightly less as orientation fluctuations often occur when rods are close to one another). A very steep gradient is then observed near the tip and on the side of the excluded volume region, where two sharp peaks are observed and are the consequence of the pairings described above: the peak at the tip corresponds to rods being attracted head-on, while the peak on the side corresponds to interactions with a slight offset. A depletion region is also observed along the horizontal axis ($z = 0$), where the black region of excluded volume is seen to extend radially: this depletion is the consequence of the repulsion that occurs when two rods are aligned side by side. Further away from the excluded volume region $p(r, z)$ quickly becomes uniform in all directions and reaches its asymptotic value of 1. Interestingly $p(r, z)$ is
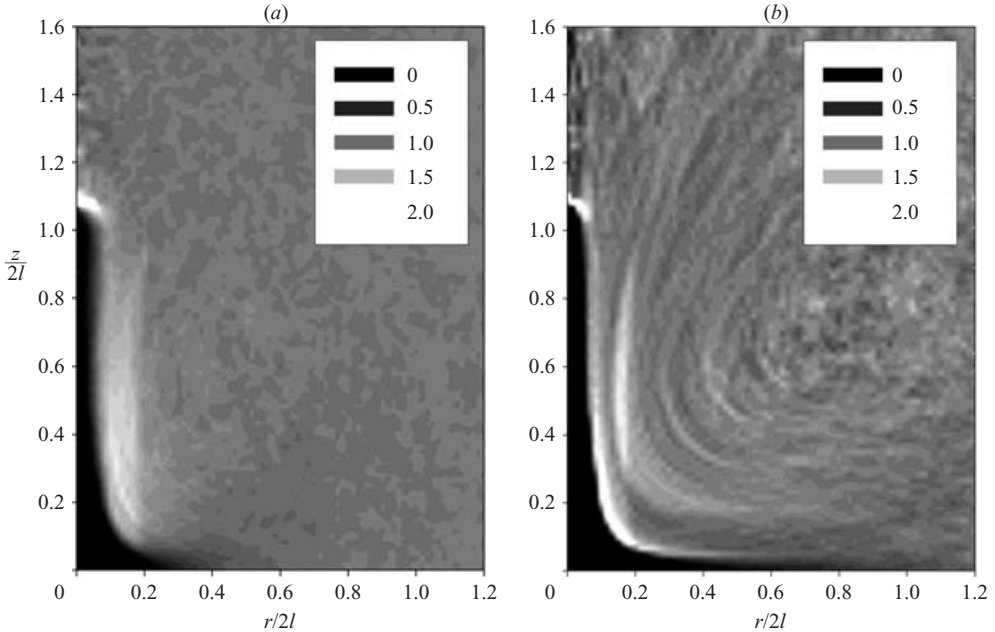
FIGURE 7. Pair distributions in a suspension of 400 rods of aspect ratio $\gamma = 10$ at infinite Péclet number, at an effective volume fraction of (*a*) $nl^3 = 0.1$, and (*b*) $nl^3 = 0.01$. The black region along the vertical axis is due to excluded volume, while the white patches around it show proof of particle pairing.

qualitatively the same at both concentrations ($nl^3 = 0.1$ and 0.01), and in particular pairing is still observed to occur even in quite dilute systems.

5.1.2. *Hydrodynamic dispersion*

The superposition of all the relative motions between the rods can be expected to lead to a diffusive behaviour at long times. This is indeed confirmed by considering mean-square displacement curves, as shown in figure 8. Initially the mean-square displacements are observed to grow quadratically, corresponding to a convective regime. However after several particle–particle interactions the motions decorrelate in time, resulting in a linear growth characteristic of diffusive processes. Hydrodynamic dispersion is a common phenomenon in non-Brownian particulate suspensions, and in particular has been well-characterized in sedimentation (e.g. Ham & Homsy 1988; Nicolai *et al.* 1995) as well as simple linear flows (e.g. Sierou & Brady 2004). While in these instances dispersion occurs relative to a mean convective motion such as settling under gravity or shear flow, the dispersion observed in figure 8 is atypical as the mean motion of the suspension is zero.

Curves such as those of figure 8 can be used to calculate effective dispersion coefficients. More precisely we define a hydrodynamic diffusion tensor $\boldsymbol{D}$ as

$$\boldsymbol{D} = \lim_{t \to \infty} \frac{1}{2} \frac{\mathrm{d}}{\mathrm{d}t} \langle (\boldsymbol{x}(t) - \boldsymbol{x}_0)(\boldsymbol{x}(t) - \boldsymbol{x}_0) \rangle. \tag{5.1}$$

As is obvious from figure 8 the tensor $\boldsymbol{D}$ is anisotropic, and for symmetry reasons $D_{xx} = D_{yy}$. Simulations also show that off-diagonal components are zero: $D_{ij} = 0$ for $i \neq j$. Numerical results for D_{xx} and D_{zz} at various concentrations and aspect ratios are
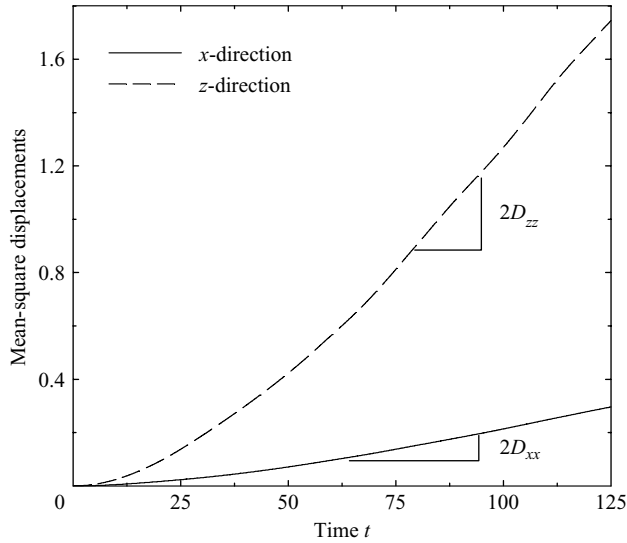
FIGURE 8. Mean-square displacements $\langle (x - x_0)^2 \rangle$ and $\langle (z - z_0)^2 \rangle$ in the x- and z-directions as a function of time, in a suspension of 400 rods of aspect ratio $\gamma = 20$ at an effective volume fraction of $nl^3 = 1$. The initial quadratic (convective) growth gives way to a diffusive regime, from which hydrodynamic dispersion coefficients can be inferred: $\langle (x - x_0)^2 \rangle \sim 2D_{xx}t$, $\langle (z - z_0)^2 \rangle \sim 2D_{zz}t$.
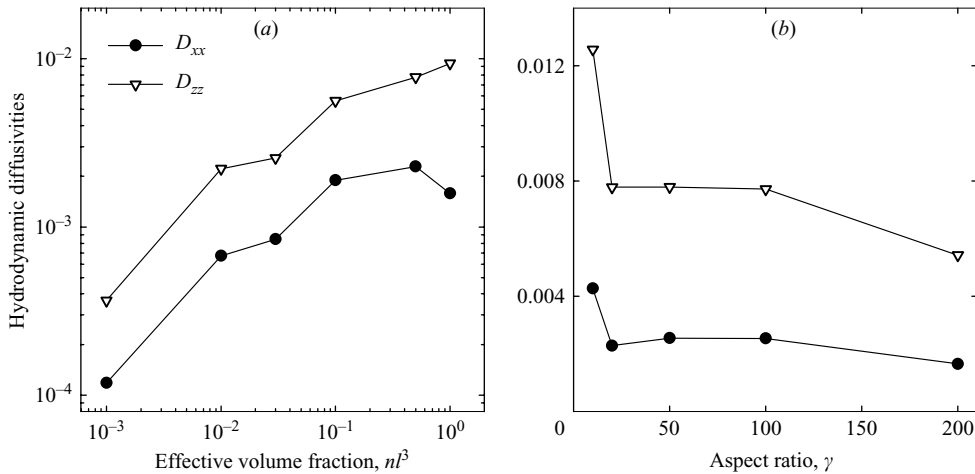

FIGURE 9. Hydrodynamic diffusivities at infinite Péclet number in the directions parallel (z-direction) and perpendicular (x-direction) to the electric field, as a function of (a) the effective volume fraction nl^3 for rods of aspect ratio $\gamma = 20$, and (b) the rod aspect ratio γ at $nl^3 = 0.1$. The results were obtained in suspensions of 400 rods.

shown in figure 9, where $\boldsymbol{D}$ is made dimensionless by $\varepsilon E_\infty^2 l^2 / \mu$. The dependence on the effective volume fraction nl^3 is shown in figure 9(a), where we see that the diffusivities increase with concentration, as a result of stronger hydrodynamic interactions. The ratio D_{zz}/D_{xx} of the diffusivities parallel and perpendicular to the direction of the electric field is roughly equal to 3.5 and approximately constant over three decades
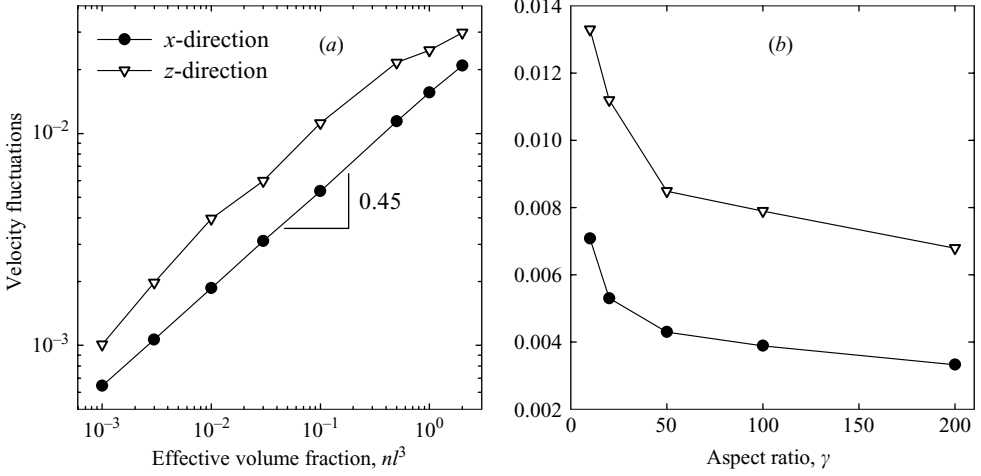
FIGURE 10. Velocity fluctuations (standard deviation of the rod velocities) at infinite Péclet number in the directions parallel (z-direction) and perpendicular (x-direction) to the electric field, as a function of (a) the effective volume fraction nl^3 for rods of aspect ratio $\gamma = 20$, and (b) the rod aspect ratio γ at $nl^3 = 0.1$. The results were obtained in suspensions of 400 rods.

of concentration. The dependence on the rod aspect ratio is shown in figure 9(b). It is observed to be rather weak except at very low values of γ, at which the validity of the slender-body approximation used in the simulations becomes questionable. As γ increases, the diffusivities decrease slightly at a fixed nl^3: hydrodynamic interactions indeed become weaker at very high aspect ratio, as can be seen for instance from equation (3.4).

5.1.3. *Velocity statistics*

We also characterize the velocity fluctuations in the suspension, which are another consequence of the relative motions between the rods. Figure 10 shows the standard deviations σ_{u_x} and σ_{u_z} of the rod velocities in the x- and z-directions at various concentrations and rod aspect ratios. Note that these are typically very weak in the dilute regime, because of the relatively rapid decay as $1/r^2$ of the interactions (compared to $1/r$ in sedimentation for instance, where very strong fluctuations arise). As shown in figure 10(a) the velocity fluctuations increase with concentration according to a power law:

$$\sigma_{u_x}, \sigma_{u_z} \sim \frac{2l\varepsilon E_\infty^2}{\mu}(nl^3)^{0.45}, \tag{5.2}$$

and the ratio of the fluctuations parallel and perpendicular to the direction of the electric field is again approximately constant and equal to $\sigma_{u_z}/\sigma_{u_x} \approx 1.8$, which is of the order of the square root of the ratio of the diffusivities. As in the case of the diffusivities, figure 10(b) shows that the dependence of velocity fluctuations on the rod aspect ratio is weak, except at very low values of γ.

5.2. *Finite Péclet number*

5.2.1. *Orientation statistics*

We now consider the effects of Brownian motion, which introduces both rotational and translational diffusion. Typical particle distributions at various values of the Péclet number (i.e. for various electric field strengths) are shown in figure 11. When
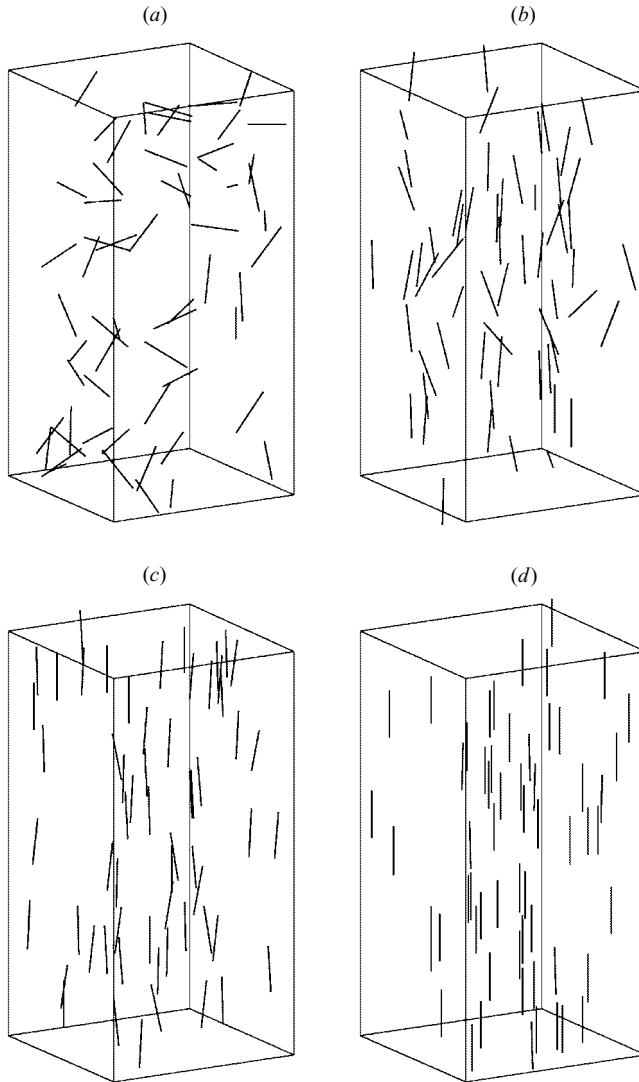
(*a*)   (*b*)

(*c*)   (*d*)

FIGURE 11. Typical particle distributions at steady state in suspensions of 60 rods of aspect ratio $\gamma = 20$, at an effective volume fraction of $nl^3 = 0.05$, and at various electric field strengths: (*a*) $Pe = 0$ (no electric field), (*b*) $Pe = 100$, (*c*) $Pe = 1000$, and (*d*) $Pe = \infty$ (no Brownian motion).

no field is applied ($Pe = 0$), the rods assume random positions and orientations, and as the Péclet number increases the alignment of the rods in the direction of the field becomes stronger. As already discussed in §5.1, the alignment is almost perfect in the infinite Péclet number limit where Brownian motion is negligible.

The dependence of the orientation of the rods on the electric field strength is made more quantitative in figure 12, which shows simulated orientation distributions $\Psi(\phi)$ at various values of Pe, where ϕ denotes the angle between the directions of the electric field and of the rods, and where the following normalization was used:

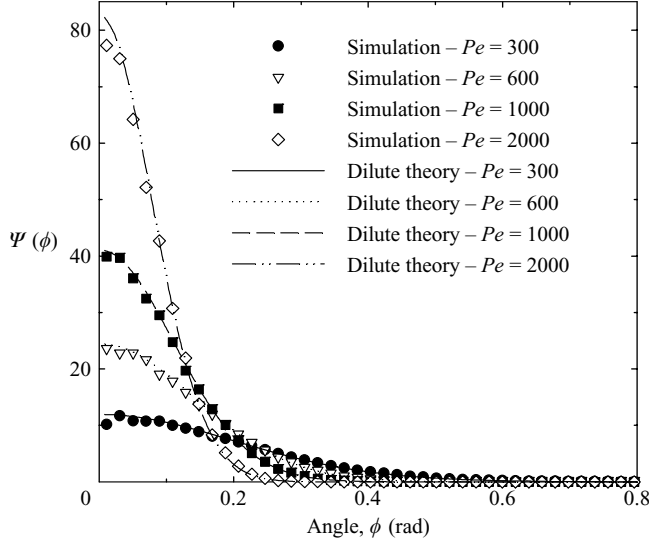$$\int_0^\pi \Psi(\phi) \sin \phi \, \mathrm{d}\phi = 1. \tag{5.3}$$

FIGURE 12. Orientation distributions $\Psi(\phi)$ at various Péclet numbers in suspensions of rods of aspect ratio $\gamma = 20$ at an effective volume fraction of $nl^3 = 0.05$, obtained from simulations (symbols) and from the dilute theory of equation (5.6) (lines).

Figure 12 also compares the simulation results to an analytical solution for the orientation distribution in the limit of infinite dilution. Indeed, if the effects of hydrodynamic interactions on orientations can be neglected, the probability density function $\Psi(\boldsymbol{p})$ for the orientation vector $\boldsymbol{p}$ of a given rod satisfies the following Fokker–Planck equation (e.g. Doi & Edwards 1986):

$$\frac{\partial \Psi}{\partial t} + \nabla_{\boldsymbol{p}} \cdot (\dot{\boldsymbol{p}}\Psi) - \nabla_{\boldsymbol{p}} \cdot (D_r \nabla_{\boldsymbol{p}}\Psi) = 0, \tag{5.4}$$

where $\nabla_{\boldsymbol{p}}$ is the differential operator in orientational space (e.g. Advani & Tucker 1987); $\dot{\boldsymbol{p}}$ denotes the rotational velocity of the rod induced by the electric field and is given by equations (2.27) and (4.3), and $D_r = 3kT \log 2\gamma / 8\pi\mu l^3$ is the Brownian rotational diffusivity of the rod. At steady state the distribution only depends on the angle ϕ, and equation (5.4) reduces to

$$\frac{\partial}{\partial \phi}\left(\frac{\varepsilon}{4\mu}G_\perp G_\parallel \sin 2\phi\, \Psi(\phi)\right) + \frac{3kT \log 2\gamma}{8\pi\mu l^3}\frac{\partial^2}{\partial\phi^2}\Psi(\phi) = 0, \tag{5.5}$$

the solution of which is a Boltzmann distribution:

$$\Psi(\phi) = A\exp\left(\frac{Pe}{96}\,G_\parallel G_\perp \cos 2\phi\right). \tag{5.6}$$

The constant A is easily determined to satisfy the normalization condition of equation (5.3). As shown in figure 12, the orientation distributions present a peak near $\phi = 0$, which becomes sharper as the electric field increases. Excellent agreement between the simulated results and the exact solution for infinite dilution is observed at the concentration shown, although larger departures can be expected at higher concentrations.

The evolution to steady state for the orientation distributions is illustrated in figure 13, which shows the time evolution of the second moment $\langle p_z p_z \rangle$ of the
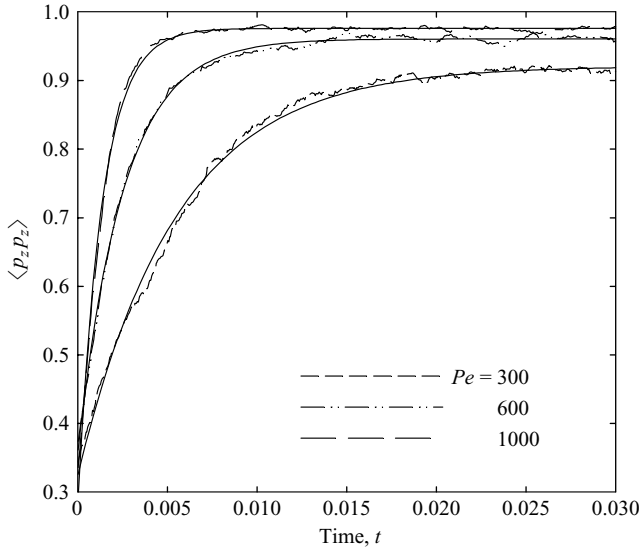
FIGURE 13. Evolution of the second moment $\langle p_z p_z \rangle$ of the z-component of the rod orientation vectors after application of an electric field in Brownian suspensions of rods of aspect ratio $\gamma = 20$ at an effective volume fraction of $nl^3 = 0.05$. The plot shows both simulations data (dashed lines) and exponential fits (full lines) at various electric field strengths.

z-component of the rod orientation vectors, where the electric field is suddenly applied at $t = 0$. Initally the rod orientations are random owing to Brownian motion, hence the value of $1/3$; as time goes on the rods align with the field, resulting in the steady increase of $\langle p_z p_z \rangle$. A plateau is finally reached, the value of which indicates the degree of alignment in the suspension. As already observed in figure 12, the alignment is stronger at high Péclet numbers. The characteristic time for the alignment also depends on the electric field strength, and is observed to be shorter at high Péclet numbers.

5.2.2. *Pair probabilities*

We also discuss the effects of Brownian motion on the particle pairing previously described in §5.1.1. Figure 14 shows simulated pair distribution functions in Brownian suspensions at the same aspect ratio and concentration as in figure 7(a), for various values of the Péclet number. When no field is applied ($Pe = 0$), the rods assume random orientations and positions resulting in the isotropic pair distribution of figure 14(a): a depleted region of spherical shape and characteristic size l exists near the origin owing to excluded volume, beyond which the pair distribution rapidly reaches its asymptotic value of 1. When a weak field is applied (e.g. $Pe = 100$, figure 14b), the depletion region is distorted and stretches in the direction of the field, as a result of the alignment of the rods; yet the pair distribution remains qualitatively very similar to the case $Pe = 0$, and in particular no pairing is observed. Pairing only appears at much higher values of the Péclet number, as shown in figures 14(c) and 14(d): beyond $Pe = 1000$, peaks in the pair distributions surround the tip of the depletion region, which is now much narrower. At $Pe = 5000$ the effects of Brownian diffusion become negligible and the pair distribution is qualitatively similar to the non-Brownian case of figure 7.
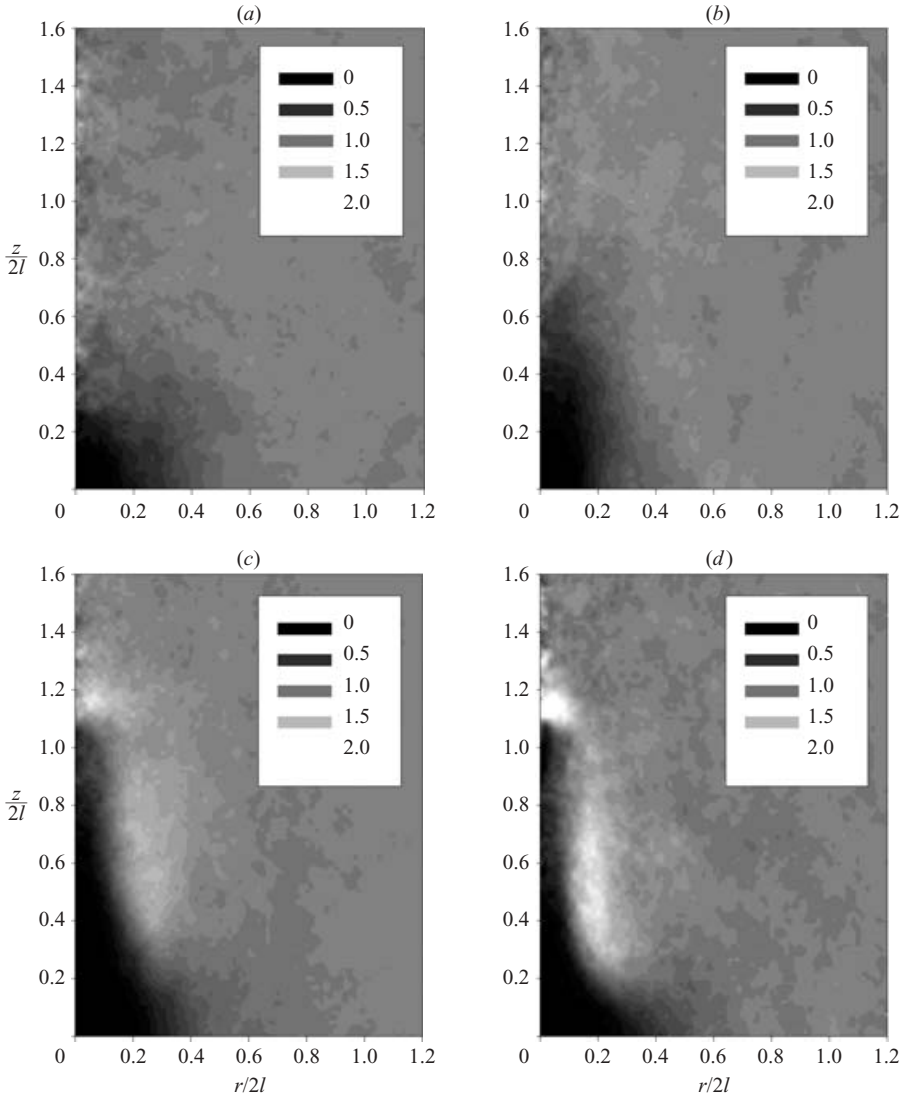
FIGURE 14. Pair distributions in Brownian suspensions of 60 rods of aspect ratio $\gamma = 10$ at an effective volume fraction of $nl^3 = 0.1$, and at various electric field strengths: (a) $Pe = 0$ (no electric field), (b) $Pe = 100$, (c) $Pe = 1000$, and (d) $Pe = 5000$.

6. Concluding remarks

We have presented a study of the behaviour of dispersions of infinitely polarizable slender rods in an electric field, with and without Brownian motion. We first derived a simple model for particle motions and interactions, based on the thin double layer approximation and on slender-body theory, and valid for high-aspect-ratio particles. In particular, we showed that the effects of the nonlinear induced-charge electrophoretic flows on the particle surfaces can be modelled by a linear slip velocity along the rod axes, which causes the alignment of the rods in the direction of the electric field and induces linear distributions of point-force singularities. These distributions of point forces drive stresslet disturbance flows in the surrounding fluid, resulting in

hydrodynamic interactions. We then applied this slender-body model to study the relative motions of two suspended rods: approximate expressions were calculated for the relative velocity between two aligned rods, and a semi-analytical solution was obtained for the pair distribution function in a dilute dispersion. The presence of a peak in the pair distribution function suggests that particle pairing can be expected as result of the relative motions.

More detailed information on the particle dynamics was then obtained using numerical simulations. We have described a simulation method based on interactions between slender bodies, which includes both far-field and near-field hydrodynamic interactions as well as Brownian motion. Simulations at infinite Péclet number (negligible Brownian motion) confirmed the existence of pairing, and qualitative agreement was obtained between the semi-analytical and simulated pair distribution functions. The superposition of the disturbance flows induced by the rods was also shown to result in a diffusive motion at long times, and hydrodynamic dispersion coefficients were calculated. Finally the effects of Brownian diffusion were discussed, and we showed that both particle alignment and pairing are made weaker by Brownian motion.

The results discussed in this paper have implications for colloid science and microfluidics, where electric fields are commonly used to control the orientation of anisotropic particles (e.g. Han & Yang 1996; van der Zande, Koper & Lekkerkerker 1999). While previous studies have focused on the determination of the rotational motion of the particles while overlooking hydrodynamic interactions, this work demonstrates that the latter can be relevant even in the case of uncharged particles, as relative motions created by induced-charge electrophoresis can lead to a non-random, possibly non-uniform microstructure.

Our discussion has focused on neutrally buoyant particles in the bulk of a suspension, an ideal situation which allowed us to isolate the effects of induced-charge electrophoresis, but which may seldom occur in practical situations. In particular, metallic colloids are typically non-neutrally buoyant, and settling under gravity may lead to interesting phenomena. Sedimenting suspensions of anisotropic particles such as rods and disks have been known to undergo a concentration instability, by which a well-mixed suspension develops inhomogeneities as a result of the coupling between the translational and rotational motions of the particles (e.g. Koch & Shaqfeh 1989; Butler & Shaqfeh 2002; Saintillan, Shaqfeh & Darve 2006; Metzger, Guazzelli & Butler 2005). Both induced-charge electrophoresis and Brownian diffusion may disrupt this coupling and prevent the instability from developing. The effects of confinement may also be significant in some applications, notably in microfluidic devices: interactions with solid boundaries are therefore worthy of interest, and will be the focus of our future work.

Appendix A. Pair interactions by the method of reflections.

This appendix uses the method of reflections (Kim & Karrila 1991) combined with multipole expansions to analytically derive an asymptotic expression for the relative motion between two aligned rods as a series in powers of $l/|\boldsymbol{x}|$. Note that a similar series can also be obtained by expanding equations (3.3)–(3.5); however the method

of reflections provides an intuitive justification for these equations, and does not make any assumptions on the linearity or direction of the force distributions along the rods.

A.1. *Zeroth-order velocity*

We consider the situation of figure 4 where the two rods are aligned in the direction of the electric field and the first rod is located at the origin. The first step of the method of reflections consists of determining the linear velocity of the second rod placed in the electrophoretic disturbance field that the first rod would create if it were by itself. This disturbance field is that induced by the linear force distribution of equation (2.39), which for an aligned rod simplifies to

$$f_1^{(0)}(s_1) = -\frac{2\pi\varepsilon s_1}{\log 2\gamma} G_\parallel^2 E_\infty^2 \, p. \tag{A 1}$$

From equation (2.30) the disturbance velocity at an arbitrary position x is

$$u_1^{(0)}(x) = \frac{1}{8\pi\mu} \int_{-l}^{l} K(x - s_1 p) \cdot f_1^{(0)}(s_1) \, \mathrm{d}s_1. \tag{A 2}$$

Expanding $K(x - s_1 p)$ in a Taylor series around $s_1 = 0$, and substituting equation (A 1) for the force distribution, we can express the disturbance velocity as

$$u_1^{(0)}(x) = \frac{\varepsilon G_\parallel^2 E_\infty^2}{4\mu \log 2\gamma} \left[\frac{2l^3}{3} p \cdot \nabla K(x) + \frac{l^5}{15} ppp : \nabla\nabla\nabla K(x) \right] \cdot p + O(|x|^{-6}). \tag{A 3}$$

Note that only odd derivatives appear in the expansion owing to the linearity of the force distribution. Introducing the notation $\cos \Theta = (x \cdot p)/|x|$, explicit evaluation of the derivatives yields

$$p \cdot \nabla K(x) \cdot p = (1 - 3\cos^2 \Theta) \frac{x}{|x|^3}, \tag{A 4}$$

$$ppp : \nabla\nabla\nabla K(x) \cdot p = (-9 + 90\cos^2 \Theta - 105\cos^4 \Theta) \frac{x}{|x|^5}$$
$$+ (-18\cos \Theta + 30\cos^3 \Theta) \frac{p}{|x|^4}. \tag{A 5}$$

The translational velocity of the second rod placed in the disturbance field $u_1^{(0)}$ is then given by equation (2.26):

$$U_2^{(0)} = \frac{1}{2l} \int_{-l}^{l} u_1^{(0)}(x_2 + s_2 p) \, \mathrm{d}s_2. \tag{A 6}$$

This time, expanding $u_1^{(0)}(x_2 + s_2 p)$ in a Taylor series about $s_2 = 0$, we find

$$U_2^{(0)} = u_1^{(0)}(x_2) + \frac{l^2}{6} pp : \nabla\nabla u_1^{(0)}(x_2) + O(|x_2|^{-6}). \tag{A 7}$$

Substituting the expression found for $u_1^{(0)}$ (equation (A 3)), we obtain the velocity of the second rod as

$$U_2^{(0)} = \frac{\varepsilon G_\parallel^2 E_\infty^2 l}{6\mu \log 2\gamma} \left[(1 - 3\cos^2 \Theta) \frac{xl^2}{|x|^3} + \frac{4}{5}(-3 + 30\cos^2 \Theta - 35\cos^4 \Theta) \frac{xl^4}{|x|^5} \right.$$
$$\left. + \frac{4}{5}(-6\cos \Theta + 10\cos^3 \Theta) \frac{pl^4}{|x|^4} \right] + O(|x|^{-6}), \tag{A 8}$$

where we have used $x_2 = x$. Similarly, $u_1^{(0)}$ induces a rotation of the second rod at an angular velocity given by equation (2.27):

$$\boldsymbol{\Omega}_2^{(0)} = \frac{3}{2l^3} \int_{-l}^{l} s_2 \boldsymbol{p} \times \boldsymbol{u}_1^{(0)}(x_2 + s_2 \boldsymbol{p}) \, \mathrm{d}s_2, \tag{A 9}$$

or, upon expansion of $u_1^{(0)}(x_2 + s_2 \boldsymbol{p})$ about $s_2 = 0$:

$$\boldsymbol{\Omega}_2^{(0)} = \boldsymbol{p} \times \left(\boldsymbol{p} \cdot \nabla \boldsymbol{u}_1^{(0)}(x_2) + \frac{l^2}{10} \boldsymbol{ppp} : \nabla\nabla\nabla \boldsymbol{u}_1^{(0)}(x_2) \right) + O(|x_2|^{-6}). \tag{A 10}$$

All calculations done, the zeroth-order angular velocity is found to be

$$\boldsymbol{\Omega}_2^{(0)} = \frac{\varepsilon G_\parallel^2 E_\infty^2 l}{2\mu \log 2\gamma} \left[(-3\cos\Theta + 15\cos^3\Theta) \frac{\boldsymbol{p} \times \boldsymbol{x} l^3}{|x|^4} \right.$$

$$\left. + 15(15\cos\Theta - 70\cos^3\Theta + 63\cos^5\Theta) \frac{\boldsymbol{p} \times \boldsymbol{x} l^5}{|x|^6} \right] + O(|x|^{-6}). \tag{A 11}$$

For obvious symmetry reasons, the velocity of the first rod induced by the electrophoretic flow on the second rod is the opposite of equation (A 8), while both angular velocities are the same.

A.2. *First reflection*

In addition to causing the motion of the second rod, the zeroth-order disturbance $u_1^{(0)}$ created by the first rod also induces a force distribution along the second rod, given by equation (2.29):

$$\boldsymbol{f}_2^{(1)}(s_2) = \frac{4\pi\mu}{\log 2\gamma} \left(\boldsymbol{I} - \tfrac{1}{2} \boldsymbol{pp} \right) \cdot \left[\boldsymbol{U}_2^{(0)} + s_2 \boldsymbol{\Omega}_2^{(0)} \times \boldsymbol{p} - \boldsymbol{u}_1^{(0)}(x_2 + s_2 \boldsymbol{p}) \right], \tag{A 12}$$

which creates the following disturbance flow:

$$\boldsymbol{u}_2^{(1)}(x) = \frac{1}{8\pi\mu} \int_{-l}^{l} \boldsymbol{K}(x - x_2 - s_2 \boldsymbol{p}) \cdot \boldsymbol{f}_2^{(1)}(s_2) \, \mathrm{d}s_2. \tag{A 13}$$

Expanding both $\boldsymbol{K}(x - x_2 - s_2 \boldsymbol{p})$ and $u_1^{(0)}(x_2 + s_2 \boldsymbol{p})$ in Taylor series about $s_2 = 0$ yields

$$\boldsymbol{u}_2^{(1)}(x) = -\frac{l^3}{2\log 2\gamma} \boldsymbol{p} \cdot \nabla \boldsymbol{K}(x - x_2) \cdot \left. \frac{\partial \boldsymbol{f}_2^{(1)}(s_2)}{\partial s_2} \right|_{s_2=0} + O(|x - x_2|^{-6}), \tag{A 14}$$

which convects the first rod at a velocity

$$\boldsymbol{U}_1^{(1)} = \frac{1}{2l} \int_{-l}^{l} \boldsymbol{u}_2^{(1)}(x_1 + s_1 \boldsymbol{p}) \, \mathrm{d}s_1 = \boldsymbol{u}_2^{(1)}(x_1) + O(|x_1 - x_2|^{-6}). \tag{A 15}$$

The derivatives in equation (A 14) can be calculated, and recalling that $x_2 - x_1 = x$ we find that the first reflection of the electrophoretic velocity from the second rod back to the first rod results in the following velocity:

$$\boldsymbol{U}^{(1)} = \frac{\varepsilon G_\parallel^2 E_\infty^2 l}{18\mu(\log 2\gamma)^2} (1 - 15\cos^2\Theta + 51\cos^4\Theta - 45\cos^6\Theta) \frac{\boldsymbol{x} l^5}{|x|^6} + O(|x|^{-6}). \tag{A 16}$$

For symmetry reasons the first reflection on the second rod leads to $\boldsymbol{U}_2^{(1)} = -\boldsymbol{U}_1^{(1)}$. Note that the reflected disturbance flow equation (A 13) also induces an additional angular velocity on the first rod, but this angular velocity scales as $O(|x|^{-6})$ and therefore is not computed here.

A.3. *Relative motion to order* $|\boldsymbol{x}|^{-6}$

Realizing that the relative velocity between the two rods is equal to $\boldsymbol{U} = 2\boldsymbol{U}_2$, the above derivations provide an asymptotic expansion for $\boldsymbol{U}$ valid to order $|\boldsymbol{x}|^{-6}$:

$$\boldsymbol{U} = \boldsymbol{U}^{(0)} + \boldsymbol{U}^{(1)} + O(|\boldsymbol{x}|^{-6}), \tag{A 17}$$

where

$$\boldsymbol{U}^{(0)} = \frac{\varepsilon G_\parallel^2 E_\infty^2 l}{3\mu \log 2\gamma} \left[(1 - 3\cos^2\Theta)\frac{\boldsymbol{x} l^2}{|\boldsymbol{x}|^3} + \frac{4}{5}(-3 + 30\cos^2\Theta - 35\cos^4\Theta)\frac{\boldsymbol{x} l^4}{|\boldsymbol{x}|^5} \right.$$
$$\left. + \frac{4}{5}(-6\cos\Theta + 10\cos^3\Theta)\frac{\boldsymbol{p} l^4}{|\boldsymbol{x}|^4} \right], \quad \text{(A 18)}$$

$$\boldsymbol{U}^{(1)} = \frac{\varepsilon G_\parallel^2 E_\infty^2 l}{9\mu(\log 2\gamma)^2}(1 - 15\cos^2\Theta + 51\cos^4\Theta - 45\cos^6\Theta)\frac{\boldsymbol{x} l^5}{|\boldsymbol{x}|^6}. \tag{A 19}$$

Both rods also rotate at the same angular velocity:

$$\boldsymbol{\Omega} = \frac{\varepsilon G_\parallel^2 E_\infty^2 l}{2\mu \log 2\gamma} \left[(-3\cos\Theta + 15\cos^3\Theta)\frac{\boldsymbol{p} \times \boldsymbol{x} l^3}{|\boldsymbol{x}|^4} \right.$$
$$\left. + 15(15\cos\Theta - 70\cos^3\Theta + 63\cos^5\Theta)\frac{\boldsymbol{p} \times \boldsymbol{x} l^5}{|\boldsymbol{x}|^6} \right] + O(|\boldsymbol{x}|^{-6}). \quad \text{(A 20)}$$

Higher terms in the expansions could be obtained by considering further reflections of the disturbance field and keeping additional terms in the multipole expansions. Importantly, one should note that the angular velocity is non-zero, and two rods initially aligned with the electric field will not remain so. The assumption of alignment with the field made in §3.1 is therefore not exact; yet simulations show that departures from the perfect alignment are typically quite weak. Note also that the same asymptotic expression for the relative velocity could have been obtained by expanding equation (3.5) in a Taylor series; higher-order terms however would differ, as the method of reflections can account for nonlinear force distributions, unlike the slender-body model of §3.1 (see equation (3.1)).

Appendix B. Asymptotic form of the pair distribution function

Equation (3.8) for the pair distribution $p(\boldsymbol{x})$ can be solved analytically in the far field. The leading-order term in $\boldsymbol{U}$ is radial, as shown in equation (A 18), so that in spherical coordinates (ρ, Θ) (where $\rho = |\boldsymbol{x}|$ and $\cos\Theta = (\boldsymbol{x} \cdot \boldsymbol{p})/|\boldsymbol{x}|$) equation (3.8) simplifies to

$$\frac{\varepsilon G_\parallel^2 E_\infty^2 l}{3\mu \log 2\gamma}(1 - 3\cos^2\Theta)\frac{1}{\rho^2}\frac{\partial}{\partial\rho}(\log p) = -\nabla \cdot \boldsymbol{U}. \tag{B 1}$$

It is easy to see that $\boldsymbol{U}^{(0)}$ is divergence-free, and that the leading-order term in the divergence is therefore $\nabla \cdot \boldsymbol{U}^{(1)}$. Calculating the leading-order term in $\nabla \cdot \boldsymbol{U}^{(1)}$ and integrating equation (B 1) subject to the boundary condition $p(\rho, \Theta) \to 1$ as $\rho \to \infty$ yields

$$p(\rho, \Theta) = \exp\left(-\frac{(1 - 12\cos^2\Theta + 15\cos^4\Theta)l^3}{6\log 2\gamma\rho^3}\right), \tag{B 2}$$

using equation (A 19) from the method of reflections. In particular, $p(\rho, \Theta)$ tends to 1 exponentially as $\rho \to \infty$.

REFERENCES

ADVANI, S. & TUCKER, C. 1987 The use of tensors to describe and predict fiber orientation in short fiber composites. *J. Rheol.* **31**, 751–784.

BANCHIO, A. J. & BRADY, J. F. 2003 Accelerated Stokesian Dynamics: Brownian motion. *J. Chem. Phys.* **118**, 10323–10332.

BATCHELOR, G. K. 1970 Slender-body theory for particles of arbitrary cross-section in Stokes flow. *J. Fluid Mech.* **44**, 419–440.

BATCHELOR, G. K. & GREEN, J. T. 1972 The determination of the bulk stress in a suspension of spherical particles to order c^2. *J. Fluid Mech.* **56**, 401–427.

BAZANT, M. Z. & SQUIRES, T. M. 2004 Induced-charge electrokinetic phenomena: Theory and microfluidic applications. *Phys. Rev. Lett.* **92**, 066101.

BOSSIS, G. & BRADY, J. F. 1987 Self-diffusion of Brownian particles in concentrated suspensions under shear. *J. Chem. Phys.* **87**, 5437–5448.

BRADY, J. F. & BOSSIS, G. 1988 Stokesian dynamics. *Annu. Rev. Fluid Mech.* **20**, 111–157.

BUTLER, J. E. & SHAQFEH, E. S. G. 2002 Dynamic simulations of the inhomogeneous sedimentation of rigid fibres. *J. Fluid Mech.* **468**, 205–237.

BUTLER, J. E. & SHAQFEH, E. S. G. 2005 Brownian dynamics simulations of a flexible polymer chain which includes continuous resistance and multibody hydrodynamic interactions. *J. Chem. Phys.* **122**, 014901.

CANUTO, C., HUSSAINI, M. Y., QUARTERONI, A. & ZANG, T. A. 1988 *Spectral Methods in Fluid Dynamics.* Springer.

CHEN, S. B. & KOCH, D. L. 1996 Electrophoresis and sedimentation of charged fibers. *J. Colloid Interface Sci.* **180**, 466–477.

CHWANG, A. T. & WU, T. Y. 1974 A note of potential flow involving prolate spheroids. *Schiffstech.* **21**, 19–31.

CHWANG, A. T. & WU, T. Y. 1975 Hydromechanics of low-Reynolds-number flow. Part 2. Singularity method for Stokes flow. *J. Fluid Mech.* **67**, 787–815.

CLAEYS, I. L. & BRADY, J. F. 1989 Lubrication singularities of the grand resistance tensor for two arbitrary particles. *PhysicoChem. Hydrodyn.* **11**, 261–293.

CLAEYS, I. L. & BRADY, J. F. 1993 Suspensions of prolate spheroids in Stokes flow. Part 1. Dynamics of a finite number of particles in an unbounded fluid. *J. Fluid Mech.* **251**, 411–442.

COX, R. G. 1970 The motion of long slender bodies in a viscous fluid. Part 1. General Theory. *J. Fluid Mech.* **44**, 791–810.

DOI, M. & EDWARDS, S. F. 1986 *The Theory of Polymer Dynamics.* Oxford University Press.

DUKHIN, A. S. 1986 Pair interaction of particles in electric field. 3. Hydrodynamic interaction of ideally polarizable metal particles and dead biological cells. *Colloid J. USSR* **48**, 376–381.

DUKHIN, A. S. & MURTSOVKIN, V. A. 1986 Pair interaction of particles in electric field. 2. Influence of polarization of double layer of dielectric particles on their hydrodynamic interaction in a stationary electric field. *Colloid J. USSR* **48**, 203–209.

DURLOFSKY, L. J. & BRADY, J. F. 1989 Dynamic simulation of bounded suspensions of hydrodynamically interacting particles. *J. Fluid Mech.* **200**, 39–67.

ERMAK, D. L. & MCCAMMON, J. A. 1978 Brownian dynamics with hydrodynamic interaction. *J. Chem. Phys.* **69**, 1352–1360.

FAIR, M. C. & ANDERSON, J. L. 1989 Electrophoresis of nonuniformly charged ellipsoidal particles. *J. Colloid Interface Sci.* **127**, 388–400.

FIXMAN, M. 1978 Simulation of polymer dynamics. I. General theory. *J. Chem. Phys.* **69**, 1527–1537.

FIXMAN, M. 1986 Construction of Langevin forces in the simulation of hydrodynamic interaction. *Macromolecules* **19**, 1204–1207.

GAMAYUNOV, N. I., MANTROV, G. I. & MURTSOVKIN, V. A. 1992 Study of flows induced in the vicinity of conducting particles by an external electric field. *Colloid J. USSR* **54**, 20–23.

GAMAYUNOV, N. I., MURTSOVKIN, V. A. & DUKHIN, A. S. 1986 Pair interaction of particles in electric field. 1. Features of hydrodynamic interaction of polarized particles. *Colloid J. USSR* **48**, 197–203.

GRASSIA, P. S., HINCH, E. J. & NITSCHE, L. C. 1995 Computer simulations of Brownian motion of complex systems. *J. Fluid Mech.* **282**, 373–403.

HAM, J. M. & HOMSY, G. M. 1988 Hindered settling and hydrodynamic dispersion in quiescent sedimenting suspensions. *Intl J. Multiphase Flow* **14**, 533–546.

HAN, S. P. & YANG, S.-M. 1996 Orientation distribution and electrophoretic motions of rod-like particles in a capillary. *J. Colloid Interface Sci.* **177**, 132–142.

HARLEN, O. G., SUNDARARAJAKUMAR, R. R. & KOCH, D. L. 1999 Numerical simulations of a sphere settling through a suspension of neutrally buoyant fibres. *J. Fluid Mech.* **388**, 355–388.

HASIMOTO, H. 1959 On the periodic fundamental solutions of the Stokes equations and their application to viscous flow past a cubic array of spheres. *J. Fluid Mech.* **5**, 317–328.

HENRY, D. C. 1931 The cataphoresis of suspended particles. I. The equation of cataphoresis. *Proc. R. Soc. Lond.* A **133**, 106–129.

HIEMENZ, P. C. & RAJAGOPALAN, R. 1997 *Principles of Colloid and Surface Chemistry*. Marcel Dekker.

HUNTER, R. J. 2001 *Foundations of Colloid Science*. Oxford University Press.

JENDREJACK, R. M., GRAHAM, M. D. & DE PABLO, J. J. 2000 Hydrodynamic interactions in long chain polymers: Application of the Chebyshev polynomial approximation in stochastic simulations. *J. Chem. Phys.* **113**, 2894–2900.

JONES, T. B. & WASHIZU, M. 1996 Multipolar dielectrophoretic and electrorotation theory. *J. Electrostat.* **37**, 121–134.

KIM, S. & KARRILA, S. P. 1991 *Microhydrodynamics: Principles and Selected Applications*. Butterworth-Heinemann.

KOCH, D. L. & SHAQFEH, E. S. G. 1989 The instability of a dispersion of sedimenting spheroids. *J. Fluid Mech.* **209**, 521–542.

LEVITAN, J. A., DEVASENATHIPATHY, S., STUDER, V., BEN, Y., THORSEN, T., SQUIRES, T. M. & BAZANT, M. Z. 2005 Experimental observation of induced-charge electro-osmosis around a metal wire in a microchannel. *Colloids Surf.* A **267**, 122–132.

MACKAPLOW, M. B. & SHAQFEH, E. S. G. 1998 A numerical study of the sedimentation of fibre suspensions. *J. Fluid Mech.* **376**, 149–182.

METZGER, B., GUAZZELLI, E. & BUTLER, J. E. 2005 Large-scale streamers in the sedimentation of a dilute fiber suspension. *Phys. Rev. Lett.* **95**, 164506.

MORRISON, F. A. 1970 Electrophoresis of a particle of arbitrary shape. *J. Colloid Interface Sci.* **34**, 210–214.

MURTSOVKIN, V. A. 1996 Nonlinear flows near polarized disperse particles. *Colloid J. USSR* **58**, 341–349.

NICEWARNER-PEÑA, S. R., FREEMAN, R. G., REISS, B. D., HE, L., PEÑA, D. J., WALTON, I. D., CROMER, R., KEATING, C. D. & NATAN, M. J. 2001 Submicrometer metallic barcodes. *Science* **294**, 137–141.

NICOLAI, H., HERZHAFT, B., HINCH, E. J., OGER, L. & GUAZZELLI, E. 1995 Particle velocity fluctuations and hydrodynamic self-diffusion of sedimenting non-Brownian spheres. *Phys. Fluids* **7**, 12–23.

O'BRIEN, R. W. 1983 The solution of the electrokinetic equations for colloidal particles with thin double layers. *J. Colloid Interface Sci.* **92**, 204–216.

O'BRIEN, R. W. & WARD, D. N. 1988 The electrophoresis of a spheroid with a thin double layer. *J. Colloid Interface Sci.* **121**, 402–413.

RUSSEL, W. B., SAVILLE, D. A. & SCHOWALTER, W. R. 1989 *Colloidal Dispersions*. Cambridge University Press.

SAINTILLAN, D., DARVE, E. & SHAQFEH, E. S. G. 2005 A smooth particle-mesh Ewald algorithm for Stokes suspension simulations: The sedimentation of fibers. *Phys. Fluids* **17**, 033301.

SAINTILLAN, D., SHAQFEH, E. S. G. & DARVE, E. 2006 The growth of concentration fluctuations in dilute dispersions of orientable and deformable particles under sedimentation. *J. Fluid Mech.* **553**, 347–388.

SAVILLE, D. A. 1977 Electrokinetic effects with small particles. *Annu. Rev. Fluid Mech.* **9**, 321–337.

SELLIER, A. 2000 Electrophoretic motion of a slender particle embedded in an axisymmetric electric field. *C. R. Acad. Sci. Paris* **328**, 41–46.

SHERWOOD, J. D. & STONE, H. A. 1995 Electrophoresis of a thin charged disk. *Phys. Fluids* **7**, 697–705.

SIEROU, A. & BRADY, J. F. 2001 Accelerated Stokesian Dynamics simulations. *J. Fluid Mech.* **448**, 115–146.

SIEROU, A. & BRADY, J. F. 2004 Shear-induced self-diffusion in non-colloidal suspensions. *J. Fluid Mech.* **506**, 285–314.

SMOLUCHOWSKI, M. 1903 Contribution à la théorie de l'endosmose électrique et de quelques phenomènes corrélatifs. *Bull. Intl Acad. Sci. Cracovie* **8**, 182–200.

SOLOMENTSEV, Y. & ANDERSON, J. L. 1994 Electrophoresis of slender particles. *J. Fluid Mech.* **279**, 197–215.

SOLOMENTSEV, Y. & ANDERSON, J. L. 1995 Electrophoretic transport of spheroidal colloids in nonhomogeneous electric fields. *Ind. Engng Chem. Res.* **34**, 3231–3238.

SOLOMENTSEV, Y., PAWAR, Y. & ANDERSON, J. L. 1993 Electrophoretic mobility of nonuniformly charged spherical particles with polarization of the double layer. *J. Colloid Interface Sci.* **158**, 1–9.

SQUIRES, T. M. & BAZANT, M. Z. 2004 Induced-charge electro-osmosis. *J. Fluid Mech.* **509**, 217–252.

SQUIRES, T. M. & BAZANT, M. Z. 2006 Breaking symmetries in induced-charge electro-osmosis and electrophoresis. *J. Fluid Mech.* **560**, 65–101.

STRATTON, J. A. 1941 *Electromagnetic Theory*. McGraw-Hill.

WALTON, I. D., NORTON, S. M., BALASINGHAM, A., HE, L., OVISO, D. F., GUPTA, D., RAJU, P. A., NATAN, M. J. & FREEMAN, R. G. 2002 Particles for multiplexed analysis in solution: detection and identification of striped metallic particles using optical microscopy. *Anal. Chem.* **74**, 2240–2247.

YARIV, E. 2005 Induced-charge electrophoresis of nonspherical particles. *Phys. Fluids* **17**, 051702.

YOUNGREN, G. K. & ACRIVOS, A. 1975 Stokes flow past a particle of arbitrary shape: a numerical method of solution. *J. Fluid Mech.* **69**, 377–403.

VAN DER ZANDE, B. M. I., KOPER, G. J. M. & LEKKERKERKER, H. N. W. 1999 Alignment of rod-shaped gold particles by electric fields. *J. Phys. Chem.* B **103**, 5754–5760.